Design and Testing of a GNSS Reflectometry CubeSat Payload for Monitoring Climate Change

by

Gary Chan

A thesis
presented to the University of Waterloo
in fulfillment of the
thesis requirement for the degree of
Master of Applied Science
in
Mechanical and Mechatronics Engineering

Waterloo, Ontario, Canada, 2017

Author's Declaration

I hereby declare that I am the sole author of this thesis. This is a true copy of the thesis, including any required final revisions, as accepted by my examiners.

I understand that my thesis may be made electronically available to the public.

Abstract

This thesis presents an alternative method for using reflected global navigation satellite systems (GNSS) signals as a remote sensing technology. The method aims to reduce the costs required so that the technology can be used on a CubeSat for the purpose of monitor Canadian arctic sea ice. The presence and age of sea ice can be determined by estimating the dielectric properties. In order to verify the hardware designed for this method, the system is placed on a quadcopter and flown near Columbia Lake at the University of Waterloo. Multiple sets of data are recorded and analyzed using the proposed method. The results show that the system is able to differentiate between water and land, with the potential for this method to identify and monitor sea ice in the arctic.

Acknowledgements

First and foremost, I would like to thank my supervisor Armaghan Salehian for bringing me onto this project and providing guidance and feedback even as the project encountered many setbacks. I would also like to thank the past and present members of the University of Waterloo Satellite Team: Peter Kruzlics for introducing the project and helping me get started; Shahid Haider for his prior work on the payload; Justin Robinson for his help with the many reports submitted for the project in addition to his work managing WatSat during a difficult time for the team; Graham Stonebridge, Jaimin Darji, and Shubham Singh for their contributions towards developing the payload for WatSat; Jason Pye, Dianthé van Weerden, Ryan Kinnear, Arsalan Alim, Ryan O'Leary, Aaron Zink, Anthony Duffy, Allen Zhu, Kieran Ratcliffe, Mathieu Gagne, Mike Li, Corvo Lin, Isaac Sy, and many others for their work on WatSat.

Table of Contents

List of Figures

List of Tables

List of Abbreviations

BPSK Binary Phase Shift Keying

BRCS Bistatic Radar Cross Section

COTS Commercial Off-the-Shelf

CSDC Canadian Satellite Design Challenge

CSV Comma-Separated Values

DDM Delay-Doppler Map

DSP Digital Signal Processor

ECEF Earth-Centred, Earth-Fixed

EGM Earth Gravitational Model

FPGA Field-Programmable Gate Array

GEO Geostationary Earth Orbit

GNSS Global Navigation Satellite System

GNSS-R GNSS Reflectometry

GPS Global Positioning System

IF Intermediate Frequency

IGS International GNSS Service

ITAR International Traffic in Arms Regulations

KAGO Kirchhoff Approximation - Geometric Optics

KML Keyhole Markup Language

LHCP Left-hand Circular Polarized

LEO Low Earth Orbit

LLA Latitude, Longitude, Altitude

LNA Low Noise Amplifier

MEO Medium Earth Orbit

MSS Mean Square Slope

NWPR Narrowband-Wideband Power Ratio

PARIS Passive Reflectometry and Interferometry System

PCB Printed Circuit Board

PDF Probability Density Function

PRN Pseudorandom Noise

RHCP Right-hand Circular Polarized

SBAS Satellite-Based Augmentation System

SNR Signal-to-Noise Ratio

SPM Small Perturbation Method

SSTL Surrey Satellite Technology Limited

SVN Satellite Vehicle Number

UART Universal Asynchronous Receiver/Transmitter

UK-DMC United Kingdom - Disaster Monitoring Constellation

UTC Coordinated Universal Time

WGS World Geodetic System

List of Symbols

A	Scattering area
B_N	Noise bandwidth
c	Speed of light in vacuum, 299,792,458 m/s
C/N_0	Carrier-to-noise density ratio
G_r	Receiver gain
G_t	Transmitter gain
k_B	Boltzmann constant, 1.38×10^{-23} J/K
P_r	Received power
P_t	Transmitted power
$\vec{q}$	Scattering vector
$\vec{R}$	Receiver coordinates
R_r	Distance between receiver and specular point
R_t	Distance between transmitter and specular point
$\vec{S}$	Specular point coordinates
$\vec{T}$	Transmitter coordinates
T_S	System noise temperature of receiver
γ	Elevation angle
ϵ	Dielectric constant

θ Incidence angle

λ GPS L1 wavelength, 19cm

σ^0 BRCS

τ Signal delay

ϕ Signal phase

φ Latitude

$\Re$ Fresnel reflection coefficient

Chapter 1

Introduction

1.1 Remote Sensing Using Reflected GPS Signals

Ever since the first Global Positioning System (GPS) satellite was launched in 1978, scientists have been interested in whether these signals could be used in other applications. In 1993, Martín-Neira proposed the use of reflected GPS signals for the purpose of ocean altimetry, naming this system as Passive Reflectometry and Interferometry System (PARIS)[1]. Since PARIS was introduced, there have been many experiments utilizing reflected GPS signals. Applications include ocean altimetry and wind speed measurement [2][3], sea ice sensing [4][5] and classification [6][7], and soil moisture content [8][9].

In 2002, the first reflected GPS signals were detected from space [10]. The first instrument dedicated to GNSS reflectometry (GNSS-R) was launched on the UK Disaster Monitoring Constellation (UK-DMC-1) satellite in 2003. A more advanced instrument was included on TechDemoSat-1, launched in 2014. GNSS-R is also the primary technique used in the Cyclone GNSS (CYGNSS) mission, launched in 2016 [11].

GNSS-R is a form of passive remote sensing that takes advantage of existing GNSS signals. This significantly reduces the costs associated with remote sensing systems since the system does not have to broadcast its own signal. Another advantage GNSS-R has over other remote sensing methods is that there are multiple sources for the broadcast signal, which allows remote sensing of multiple paths simultaneously. A GNSS-R system requires two antennas: a zenith-oriented antenna that receives direct signals for typical position measurements and serves as a reference signal, and a nadir-oriented antenna that receives the reflected signals for remote sensing. This is illustrated in Figure 1.1.

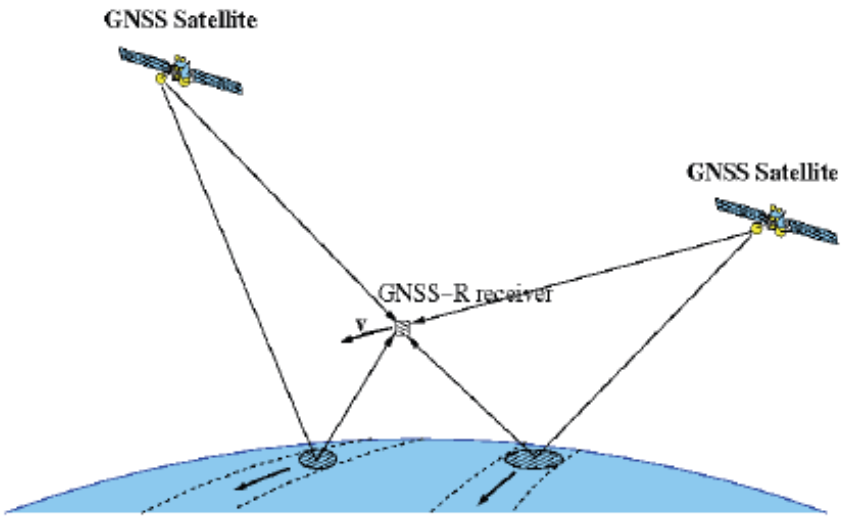

Figure 1.1: GNSS Reflectometry [12]

1.2 Remote Sensing of Arctic Sea Ice

Sea ice is an excellent indicator of climate change. As the Earth's climate continues to change, the amount of sea ice in the arctic decreases each year. By monitoring sea ice, scientists can predict the trends and effects of the global climate in the future. An example of sea ice trends is shown in Figure 1.2. At the same time, this also opens up many opportunities such as exploration, industrial development, and new shipping routes via the Northwest Passage. In order to take advantage of these opportunities, the local environment must be studied, and due to the remoteness of the arctic, satellite remote sensing is often the best choice.

There have been many satellite missions launched for the purpose of remote sensing the cryosphere. RADARSAT-1 was launched by Cananda in 1995 for Earth observation. GRACE was launched in 2002 by NASA and Germany to study gravity and the effects on water and ice distribution. ICESat was launched by NASA (National Aeronautics and Space Administration) in 2003 for measuring ice sheets.

The first use of GNSS-R for remote sensing sea ice was tested by Komjathy et al [4]. Most of the work in this area is done by Belmonte-Rivas [6][7]. The first remote sensing of sea ice from space came from the UK-DMC satellite [14]. As the technology for GNSS-R continues to develop, more satellite missions adopting the technology will be launched, including missions for monitoring climate change through the measurement of sea ice.

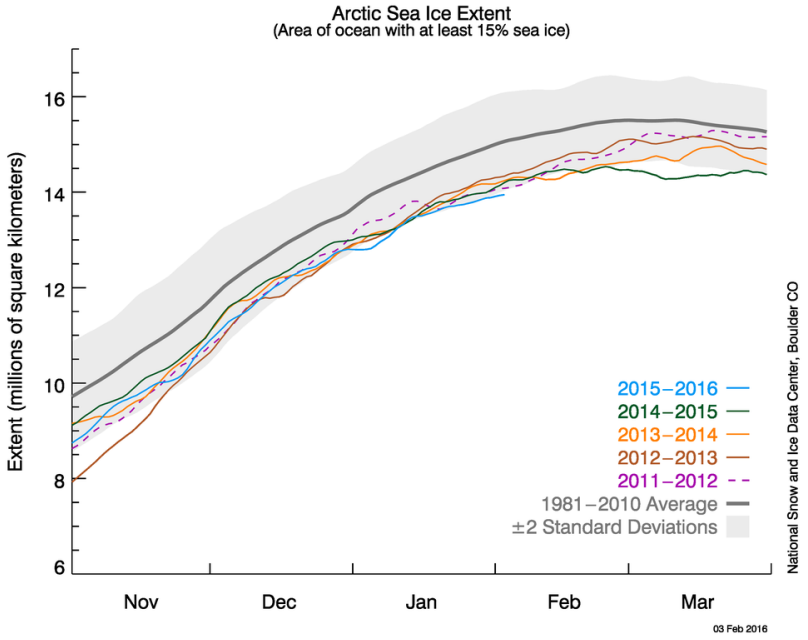

Figure 1.2: Arctic Sea Ice Extent [13]

1.3 CubeSats

The development of satellites is a long and expensive process. There are many projects where the cost or risks cannot be justified for a typical satellite. A CubeSat is a miniaturized satellite specification developed by California Polytechnic State University in 1999. The CubeSat standard was developed as a low cost solution for riskier experiments, as well as an introduction for graduate students into the process of spacecraft development. CubeSats can consist of several units (U); the most popular sizes are 1U, 2U, 3U, 6U, and 12U. One unit is 10 cm x 10 cm x 10 cm and weighs less than 1.33 kg. CubeSats often use commercial off-the-shelf (COTS) components and are typically launched as a secondary payload and in multiples. Because the CubeSat standard reduces the development and launch costs of a satellite, it serves as an attractive platform for both academic and commercial projects to perform scientific research or demonstrate new and emerging technologies. Several nations have even launched their first satellite using the CubeSat standard [15] [16] [17] [18].

Organizations around the world are funding various CubeSat projects. The Canadian Space Agency, European Space Agency, and NASA have funded CubeSats designed and built by universities. Non-governmental organizations are also getting involved in CubeSats. The Canadian Satellite Design Challenge (CSDC) is a competition for students enrolled in

Canadian universities to design a 3U CubeSat [19]. Each team must create their own mission and payload to compete for a free launch into space.

WatSat is the University of Waterloo's team competing in the CSDC. WatSat's mission is to perform GNSS-R from a CubeSat for remote sensing arctic sea ice in the Canadian archipelago.

1.4 Organization of Thesis

Chapter 2 introduces the fundamentals for GNSS reflectometry and the alternative method proposed. Chapter 3 uses the UK-DMC data to validate the proposed method. Chapter 4 describes the design of the experiment and the quadcopter setup. Chapter 5 presents the results from the quadcopter experiments. Finally, Chapter 6 summarizes the work done and the future for this research.

Chapter 2

GNSS Reflectometry

2.1 Satellite Navigation Systems

Table 2.1 summarizes the current state of existing satellite navigation systems.

Table 2.1: Satellite Navigation Systems

System	Origin	Coverage	Status	Active Satellites
GPS	United States	Global	Active	31
GLONASS	Russia	Global	Active	24
Galileo	European Union	Global	In Development	15
BeiDou	China	Global	In Development	20
NAVIC	India	Regional	Active	6
QZSS	Japan	Regional	In Development	2

GPS is the most well-known GNSS constellation. There are 32 satellites placed in six orbital planes in medium Earth orbit (MEO) approximately 20,000 km above the Earth's surface. The position of the satellites are arranged such that at least six are visible from anywhere at all times, with eight or nine usually visible for redundancy. More about GPS is described in the following section.

The Russian GLONASS constellation began development during the Cold War and was completed in 1995. A lack of maintenance because of an economic crisis resulted in the constellation reducing to six functional satellites by 2001. With the economy improving, the constellation was restored in the next decade.

GLONASS consists of 24 satellites in three orbital planes in MEO approximately 19,000 km above the Earth. The orbits are better positioned for higher latitudes where obtaining GPS signals can be an issue. Most modern GNSS receivers are capable of processing both

GPS and GLONASS signals, which allow for a quicker location fix that is also more accurate.

The Galileo constellation is currently being developed by the European Union. Galileo is designed to have higher precision than GPS, which at the time rivalled civilian GPS, resulting in pressure from the US. Combined with funding issues, development of the constellation was delayed and almost cancelled. However, both these issues were resolved and modern receivers are being developed to use both GPS and Galileo. The constellation is now expected to be fully operational in 2020. Galileo will consist of 30 satellites in three orbital planes in MEO approximately 23,000 km above the Earth.

The BeiDou constellation is a three-phase system where the first phase began with three experimental satellites. The second phase expanded to a regional system, with the third phase to achieve global coverage. The constellation will consist of five satellites in geostationary Earth orbit (GEO) and 30 satellites in MEO approximately 21,000 km above the Earth.

The NAVIC constellation consists of three satellites in GEO and four in geosynchronous orbit to provide regional coverage extending 1,500 km from India. Plans to increase the number of satellites to 11 for extended coverage.

The QZSS constellation consists of three satellites in geosynchronous orbit for coverage in the Asia-Pacific region. The constellation is a satellite-based augmentation system (SBAS) for GPS. There are also plans to increase the number of satellites to seven in the future.

2.2 Global Positioning System

In this section, the most important properties of GPS are described. The understanding of these properties is vital to GNSS-R applications.

2.2.1 Signal Structure

GPS satellites transmit two carrier frequencies: 1.57542 GHz (L1) and 1.22760 GHz (L2). Each satellite has two unique identifying codes: a coarse/acquisition (C/A) code, and an encrypted precision (P(Y)) code. These two codes are also known as pseudorandom noise (PRN) since they appear random but are generated. The C/A code is available for public use, repeats every millisecond, and is only modulated into the L1 carrier. The P(Y) code is reserved for military applications, repeats every week, and is modulated into both L1 and L2 carriers. GPS signals are right-hand circularly polarized (RHCP).

The C/A code consists of 1023 bits or chips, so the chip rate is 1.023 MHz. The C/A code sequence is unique for each GPS satellite, and each sequence is highly orthogonal to each other. The code sequences are generated using two 10-bit registers, known as G1 and G2. In each cycle, a new bit is determined using taps from the register and the entire register is shifted. G1 is tapped on bits 3 and 10, while G2 is tapped on bits 2, 3, 6, 8, 9, and 10. The output from G2 is unique to each GPS satellite and is determined by a preset delay before being combined with the output from G1 to form the C/A code.

In addition to the PRN code, there is also a navigation message modulated into the carriers. The navigation message is separated into five subframes containing time, ephemeris, and almanac information. GPS time is synchronized with Coordinated Universal Time (UTC) on January 6, 1980, and expressed as a week number and time of week in seconds. However, GPS satellites are not updated with leap seconds and is currently 18 seconds ahead of UTC time. The week number is also stored using 10 bits, which results in a rollover every 1024 weeks or 19.7 years that receivers must account for. The ephemeris contains Keplerian orbit parameters, which can be used to determine the position of transmitting satellites. These are unique to each GPS satellite, are highly detailed, and are updated frequently to maintain precision. The almanac contains less precise clock and orbit information, an ionosphere model for error correction, and satellite status information. The navigation data rate is 50 Hz.

The data and code are combined using an adder, and modulated into the carriers using binary phase shift keying (BPSK). In the case of L1, because both the C/A code and P(Y) code are modulated in the carrier, the two codes are modulated into the in-phase (I) and quadrature (Q) components so they are 90 degrees out of phase with each other. For those unfamiliar with I/Q components, every sinusoid can be written as the sum of a sine and cosine. This is especially important in signal modulation as the modulation method defines how the data is interpreted through the amplitude and phase of the signal, and can allow more bits to be encoded per symbol at the risk of a higher bit error rate. In the case of BPSK for GPS, only one bit is encoded per symbol as the quality of the data is much more important than the quantity.

On the receiver end, the signal is demodulated and then decoded using two steps: acquisition and tracking. In acquisition, the PRN of each visible satellite is determined by the receiver reproducing the C/A codes and correlating it to the received signal. By the time the signal reaches the receiver, the frequency and the code phase has likely changed, which must be considered in the C/A code replicas. Once a match is found, the signal moves to

being tracked. In tracking, the frequency and code phase is monitored with feedback loops in order to maintain synchronization with the received signal. If tracking is lost, the receiver moves back to acquisition. When the signal is successfully tracked, the navigation data can be interpreted.

2.2.2 Reference Frame

GPS uses the World Geodetic System 1984 (WGS84) as its reference system. WGS84 is a reference ellipsoid for approximating the shape of the Earth, defined by the following parameters [20]:

- Semi-major axis $a = 6,378,137.0\ m$
- Flattening $f = 1/298.257223563$
- Earth's gravitational constant $GM = 3,986,004.418 \times 10^8\ m^3/s^2$
- Earth's rate of rotation $\omega = 7.292115 \times 10^{-5}\ rad/s$

The origin [0, 0, 0] is defined as the location of the Earth's centre of mass. The z-axis is in the direction of the geographic north pole and is the axis of rotation, the x-axis is in the direction of the prime meridian normal to the z-axis, and the y-axis completes a right-handed orthogonal system. This kind of reference frame is known as an Earth-centred, Earth-fixed (ECEF) coordinate system. The MATLAB functions *lla2ecef* and *ecef2lla* are used to convert between the coordinates provided by GPS to geographical locations. The reference ellipsoid is shown in Figure 2.1.

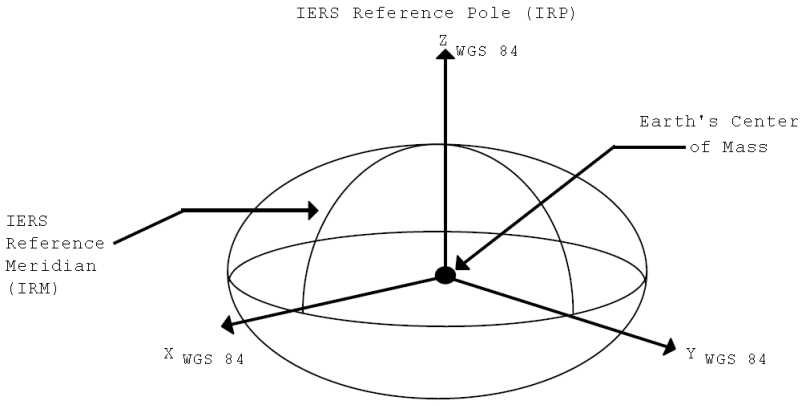

Figure 2.1: WGS84 Reference Ellipsoid [20]

However, the Earth is not a perfect ellipsoid. A better representation of the Earth is a geoid that defines variations from a perfect ellipsoid. The 1996 Earth Gravitational Model, also known as EGM96 and shown in Figure 2.2, shows the altitude correction for WGS84. The EGM96 model is comprised of a gridded data set at 15-minute intervals, for a 721 by 1441 matrix. Modern GPS receivers take into account the variation when calculating the altitude at a given position.

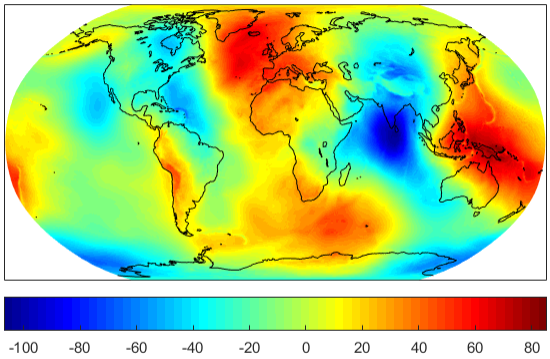

Figure 2.2: 1996 Earth Gravitational Model

2.2.3 Orbits

The International GNSS Service (IGS) provides GPS satellite ephemerides and clock information. There are three types of products available: ultra-rapid, rapid, and final. The ultra-rapid products provide near real-time orbit information and predictions, released every six hours. The reduced latency is offset by a reduction in accuracy. The rapid products are a middle solution for orbit information. These are released approximately 17 hours after the end of each day, i.e. 17:00 UTC. The accuracy provided by rapid products are good enough for most applications. The final products provide the highest accuracy for high quality applications, and are released with approximately two weeks latency. The rapid solutions are sufficient for the purpose of GNSS-R.

For all IGS products, the orbit information is provided in 15 min intervals or epochs. In order to acquire the precise GPS orbits during GNSS-R, the orbits must be interpolated. The interpolation method used is described in [21] and based on the implementation by Li [22]. Orbits are sinusoidal by nature; however, the rotating reference frame for the Earth

must be accounted for. The method accomplishes this by introducing higher order sinusoidal terms for the X and Y axes, given by Equation 2.1:

$$C = A_0 + A_1 \sin(WT) + A_2 \cos(WT) + A_3 \sin(2WT) + A_4 \cos(2WT) + ... + A_N \cos(NWT/2) \quad (2.1)$$

where W is the period equal to a sidereal day. For the eight nearest epochs, it was shown that $N = 9$ gave the best fit [21]. As this is GNSS, in addition to the three axes, the clock must also be interpolated. This is much simpler since time is linear, and is accomplished using the MATLAB function *interp1*.

2.2.4 Trilateration

Trilateration is the calculation of a position using measured distances. For GPS, this is commonly mistaken as triangulation, where a position is calculated using measured angles. In two-dimensional geometry, trilateration requires three known distances. The position is determined by drawing circles or arcs with the measured distances as the radii. The intersection of the circles or arcs is the position. Similarly, in three-dimensional geometry such as that in GPS, spheres for four known distances are used.

In GPS, the measured distance is estimated using Equation 2.2. The travel time between the transmitting satellite and the GPS receiver is multiplied by the speed of light. This is known as the pseudorange. The travel time is measured in milliseconds using the C/A code. However, each chip corresponds to 293 meters due to the chipping rate. In order to obtain a more accurate distance, the carrier phase is used. This provides a much higher accuracy for the estimated distance.

$$d = c(t_r - t_t) \quad (2.2)$$

Another problem with GPS is that there are more satellites than required for finding the position of the receiver, which produces an overdetermined system of equations with no solution. There are many ways to solve this mathematically, one of the most common being a least squares method. The least squares method attempts to reduce the error for the system of equations, represented in Equation 2.3:

$$\hat{e} = \vec{b} - A\hat{x} \tag{2.3}$$

where $\hat{e}$ is the error vector, $\vec{b}$ are the pseudoranges, and $\hat{x}$ is the receiver location. This method is described in detail in [23] and the implementation is based on code made available by the author.

2.3 Signal Propagation

The output of GPS satellites is around 500 W or 57 dBm. However, when the propagation losses are considered, the strength of GPS signals on the surface of the Earth is approximately -130 dBm. If the noise temperature is assumed to be the standard $T_S = 290K$, then the GPS signal is well below the noise floor. It is only through processing that the signal can be recovered from the noise. One of these processing steps is the coherent integration of the I/Q samples. The I/Q samples are summed over a coherent integration period, typically 1 ms, and the results are squared and summed. This increases the signal power enough for the PRN codes to become identifiable. A second integration period that is non-coherent further amplifies the signal and noise power so that the peaks can be identified in a delay waveform. The delay waveform will be discussed later in this Chapter.

The signal-to-noise ratio (SNR) for the direct signal is given by Friis transmission equation, shown in Equation 2.4, while the SNR for the reflected signal is given by the radar equation, shown in Equation 2.5.

$$SNR_D = \frac{P_d}{k_B T_S B_N} = \left(\frac{P_t G_t}{4\pi R_d^2}\right)\left(\frac{G_d \lambda^2}{4\pi}\right)\left(\frac{1}{k_B T_S B_N}\right) \tag{2.4}$$

$$SNR_R = \frac{P_r}{k_B T_S B_N} = \left(\frac{P_t G_t}{4\pi R_t^2}\right)\left(\sigma^0 A\right)\left(\frac{1}{4\pi R_r^2}\right)\left(\frac{G_r \lambda^2}{4\pi}\right)\left(\frac{1}{k_B T_S B_N}\right) \tag{2.5}$$

Because of the low altitude of the receiver relative to the altitude of GPS satellites, it can be shown using trigonometric identities that the angle difference between the two signals is negligible. Therefore, the transmitted power P_t and gain G_t can be assumed to be equal. The noise can also be assumed equal since the GPS receivers for both signals are identical. Therefore, Equation 2.4 can be substituted into Equation 2.5 to form the Equation 2.6

$$SNR_R = SNR_D \left(\frac{R_d^2}{R_t^2}\right)\left(\sigma^0 A\right)\left(\frac{1}{4\pi R_r^2}\right)\left(\frac{G_r}{G_d}\right) \tag{2.6}$$

Rearranging Equation 2.6 for the bistatic radar cross section (BRCS) σ^0, which represents the reflecting surface, results in Equation 2.7:

$$\sigma^0 = \left(\frac{SNR_R}{SNR_D}\right)\left(\frac{R_t^2}{R_d^2}\right)\left(\frac{4\pi R_r^2}{A}\right)\left(\frac{G_d}{G_r}\right) \tag{2.7}$$

2.4 Estimating SNR and C/N_0

The carrier-to-noise density ratio, or C/N_0, is a value reported by most GPS receivers. The C/N_0 is an indicator for the strength of the signal visible by the receiver, similar to SNR, and is often used in tracking GPS satellites. C/N_0 is the SNR normalized by the noise bandwidth, shown in Equation 2.8. However, according to Equation 2.7, the ratio for SNR is used to calculate the BRCS. This means that either the SNR or C/N_0 can be used, provided that the noise bandwidth is the same for both the direct and reflected signals.

$$SNR[dB] = C/N_0[dB] - B_N[dB] \tag{2.8}$$

For GPS receivers, the SNR or C/N_0 cannot be calculated using the previous equations and must be estimated using algorithms. There are many C/N_0 algorithms developed for simplicity or accuracy, but most algorithms tend to estimate SNR and convert to C/N_0 using Equation 2.8. However, there is one commonly used algorithm that estimates C/N_0 directly, known as narrowband-wideband power ratio (NWPR) [24]. This method calculates the narrowband power and wideband power of the navigation data. The algorithm is given in Equations 2.9-2.12.

$$NBP_k = \left(\sum_i^M I_i\right)^2 + \left(\sum_i^M Q_i\right)^2 \tag{2.9}$$

$$WBP_k = \sum_i^M \left(I_i^2 + Q_i^2\right) \tag{2.10}$$

$$\mu = \frac{1}{K}\sum_k^K \frac{NBP_k}{WBP_k} \tag{2.11}$$

$$C/N_0 = \frac{1}{T}\frac{\mu - 1}{M - \mu} \tag{2.12}$$

Because the algorithm is based on the I/Q samples of the GPS signal, the value for M is

based on the frequency of the navigation message bits, i.e. 20 ms. T is the non-coherent integration time, often set to 1 second. Therefore, there are a total of 50 navigation bits in the integration time, or $K = 50$. This algorithm assumes that the signal is coherent enough for the navigation bits to be obtainable.

For signals that do not remain coherent enough for NWPR to work, another solution is to simply calculate the signal power and noise power. The signal power can be taken as the peak power with the noise power removed, and the noise power can be taken as the power preceeding the peak of a delay waveform. This is shown in Equation 2.13

$$SNR = \frac{P_s - P_n}{P_n} \tag{2.13}$$

2.5 Specular Locations

Once the positions of the transmitting satellites and receiver are calculated, the location of the specular point can then be determined using geometry. The implementation is based on code used in Gleason's Ph.D. dissertation [25] and is documented in detail in [14]. The location of the specular points must satisfy the following conditions:

1. Must be the shortest path
2. Must be constrained to the Earth's surface
3. Must satisfy Snell's law, where the incident angle must be equal to the reflected angle

The path is defined as:

$$P(\vec{S}) = \left\|\vec{T} - \vec{S}\right\| + \left\|\vec{R} - \vec{S}\right\| \tag{2.14}$$

Iterating on $\vec{S}$ using Equations 2.15 and 2.16 and gain K results in Equation 2.14 converging to a minimum.

$$d\vec{S} = \frac{\vec{T} - \vec{S}}{\left\|\vec{T} - \vec{S}\right\|} + \frac{\vec{R} - \vec{S}}{\left\|\vec{R} - \vec{S}\right\|} \tag{2.15}$$

$$\vec{S}_{temp} = \vec{S} + Kd\vec{S} \tag{2.16}$$

The constraint onto the Earth's surface is reapplied after each iteration using Equations 2.17 and 2.18

$$\vec{S}_{new} = r\frac{\vec{S}_{temp}}{\left\|\vec{S}_{temp}\right\|} \tag{2.17}$$

$$r = a\sqrt{\frac{1-e^2}{1-e^2\cos^2(\varphi)}} \tag{2.18}$$

where e is the WGS84 eccentricity and r is the new radius. In the case of specular points on land, an elevation offset is applied to Equation 2.17.

2.6 Roughness and Scattering Area

The smoothness or roughness of a surface is relative to the wavelength of the incident wave. A surface can be considered smooth if the phase difference of two reflected rays is below a threshold $\Delta\phi$. The phase difference is linked to the surface height variation by the following equation:

$$\Delta h = \frac{\lambda\Delta\phi}{4\pi\cos\theta} \tag{2.19}$$

The Rayleigh criterion defines this phase threshold as $\Delta\phi = \pi/2$, while the Fraunhofer criterion defines the phase threshold as $\Delta\phi = \pi/8$. Figure 2.3 shows the height variation thresholds against incidence angle for various phase thresholds.

The scattering area or glistening zone is difficult to determine exactly and is affected by many different factors. However, there is an upper and lower bound for the possible scattering area. The upper bound is determined by the autocorrelation of the GPS PRN code. If the delay caused by the extra distance in the reflected path exceeds one code chip, the autocorrelation value changes, resulting in tracking loss of the GPS satellite. The one-chip delay forms an ellipse around the specular reflection point, known as the first isorange ellipse. The equations for this ellipse are given by the following:

$$a = \sqrt{\frac{2hc\tau}{\sin^3\gamma}} \tag{2.20}$$

$$b = \sqrt{\frac{2hc\tau}{\sin\gamma}} \tag{2.21}$$

where τ is the number of chips and γ is the elevation angle. The first isorange ellipse is given using $\tau = 1$.

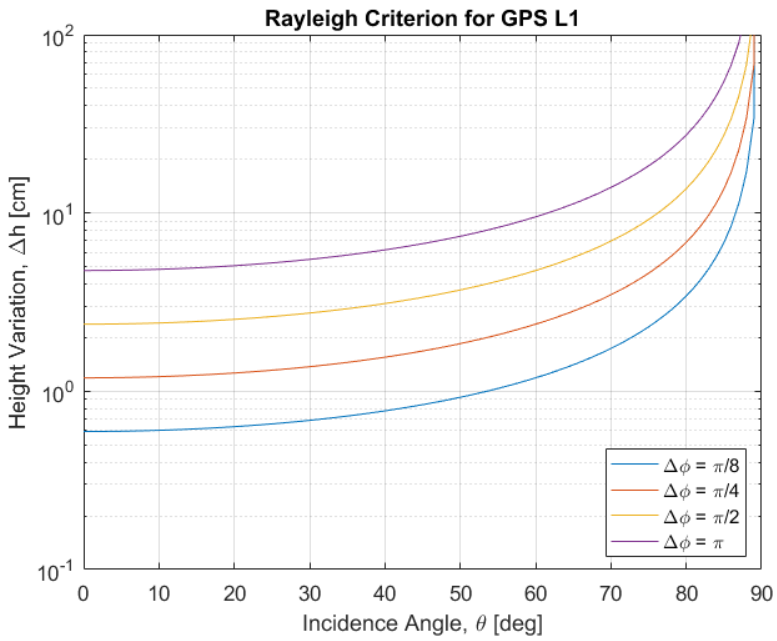

Figure 2.3: Roughness Thresholds for GPS L1

As the surface roughness decreases, the scattering area also shrinks closer around the specular point. Most of the scattering then occurs within the first Fresnel zone [26]. This area is similar to the first isorange ellipse, approximating $c\tau$ with $\lambda/2$ [9]. The equations are given by the following [27][28]:

$$b = \sqrt{\frac{\lambda h}{\sin\gamma} + \left(\frac{\lambda}{2\sin\gamma}\right)^2} \tag{2.22}$$

$$a = \frac{b}{\sin\gamma} \tag{2.23}$$

The two ellipses presented provide an upper and lower bound for the scattering area estimate. However, the actual scattering area is unknown and will vary with the reflecting surface. In order to achieve realistic results, an area adjustment factor is applied to one of the bounding area ellipses for the analysis.

2.7 Electromagnetic Scattering Models

Electromagnetic (EM) scattering models are used to characterize the interaction of EM waves on a surface. This is often represented by the BRCS as a function of the incident and scattered

fields. There are two classic models for EM scattering: Kirchhoff Approximation (KA) and Small Perturbation Method (SPM). KA is also known as the tangent plane approximation due to the assumption that all scattered EM fields are locally specular and independent of other points on the scattering surface. This also means that the surface roughness is large relative to the wavelength. It is not possible to produce an analytic solution without making additional assumptions for simplification, such as Geometric Optics or Physical Optics. The Geometric Optics assumption (KAGO) assumes the phase component is stationary and only takes into account well-oriented facets. The Physical Optics assumption accounts for the entire scattering surface, but assumes the surface slopes are small. KAGO is illustrated in Figure 2.4.

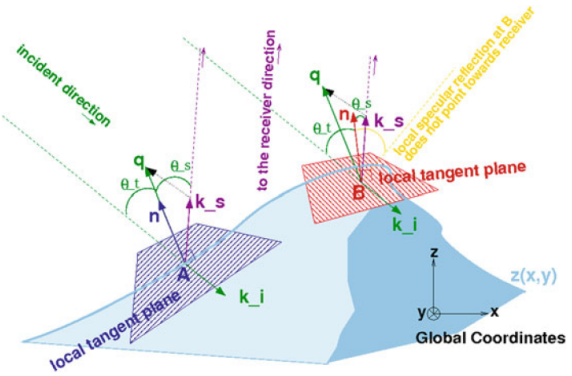

Figure 2.4: Kirchhoff Approximation Using Geometric Optics [29]

SPM is defined as a partial differential equation boundary value problem and attempts to solve using a perturbation series. This method is useful for surfaces with small height variations and accounts for Bragg scattering effects. The zero order solution represents a planar interface, while a first order solution is sufficient for incoherent scattered fields. As with most series, the inclusion of higher order terms produce more accurate solutions.

There are many other methods designed to combine the two classic models for a more accurate representation of EM scattering. The Integral Equation Method is one such method that iterative calculates the charges on a surface. This produces a very accurate result but is computationally expensive, and therefore it is usually served as a reference for other models. The Two-Scale Composite Model is also a combination of the two classic models that adds the effect of large-scale roughness with small-scale effects. However, the boundary between large-scale and small-scale is difficult to define, and the final result is not an accurate representation of real surfaces. The Small Slope Approximation is another method that attempts to combine KAGO and SPM. The assumption made for this method is that the slopes of the roughness

is small compared to the incident and scattering angles. To summarize, the surface height, incidence angles, and wavelengths must be considered when selecting a scattering model to ensure its validity.

KAGO is one of the most commonly used models in GNSS-R. It has been shown that the BRCS can be expressed as [30]:

$$\sigma^0 = \pi \left|\Re\right|^2 \frac{\vec{q}^4}{q_z^4} PDF\left(-\frac{\vec{q}_\perp}{q_z}\right) \tag{2.24}$$

where $\vec{q}_\perp$ is the projection of $\vec{q}$ on the x-y plane, q_z is the projection of $\vec{q}$ on the z-axis (normal to the surface), and PDF is the probability density function of the surface slopes, typically represented with a Gaussian distribution. The scattering vector $\vec{q}$ is defined as:

$$\vec{q} = \frac{2\pi}{\lambda}(\hat{u}_{ref} - \hat{u}_{inc}) \tag{2.25}$$

where $\hat{u}_{ref}$ and $\hat{u}_{inc}$ are unit vectors in the reflected and incident directions respectively. The PDF can be simplified to an omni-directional distribution, but for the most accurate results should be bivariate. The variance in the two directions of the distribution can be represented by the mean square slope or mss and written as:

$$PDF = \frac{1}{2\pi mss} \exp\left(-\frac{(\vec{q}_\perp/q_z)^2}{2mss}\right) \tag{2.26}$$

Equation 2.26 is then used to link the BRCS from Equation 2.7 to the scattering surface via the Fresnel reflection coefficient $\Re$, which can be solved for by inverting the KAGO model. Note that the value of $\Re$ must be between 0 and 1.

2.8 Dielectric Properties of Sea Ice

Sea ice can be classified by the concentration, thickness, or age. A simple way for classification is described by the World Meteorological Organization [31] as the following:

- New Ice: less than 10 cm thick
- Young Ice: 10-30 cm thick
- Thin First Year Ice: 30-70 cm thick
- First Year Ice: 70-200 cm thick

- Multi-year Ice: greater than 200 cm thick

In general, as sea ice grows, the salinity decreases and snow cover increases. Both of these factors have an effect on the interaction between sea ice and the L-band signals of GPS.

The Fresnel reflection coefficient is determined by the properties of two media. For this application, the transition occurs from air to sea ice. It is well known that the refractive index of air is approximately $n = 1$, whereas the index of sea ice is approximated by $n = \sqrt{\epsilon}$, where ϵ is the complex dielectric constant. The value of ϵ varies significantly with the type of sea ice. This topic has been studied in depth over a large range of frequencies for modelling sea ice [32]. One such model uses the brine volume V_b in parts per thousand (‰). For example, the complex dielectric constant can be linear approximated at 1 GHz as [5]:

$$\epsilon' = 3.12 + 0.009V_b \tag{2.27}$$

$$\epsilon'' = 0.04 + 0.005V_b \tag{2.28}$$

where ϵ' and ϵ'' are the real and imaginary components of ϵ, and $V_b \leq 70‰$. For comparison, the complex dielectric constant of open water is around $\epsilon = 80 + j30$. The expected range of values for the dielectric constants of different surfaces are shown in Table 2.2 [33].

Table 2.2: Dielectric Constants at GPS L1

Terrain	Range	Comments
Water	70-80	At 20°C, varies with salinity and temperature
Land	3-30	Varies with moisture content
Ice	∼3	Fresh water, sea ice similar to fresh water ice at GPS L1

The Fresnel reflection coefficient is also dependent on the incident angle and polarization of the wave. These are given by:

$$\Re_{HH} = \frac{\cos\theta - \sqrt{\epsilon - \sin^2\theta}}{\cos\theta + \sqrt{\epsilon - \sin^2\theta}} \tag{2.29}$$

$$\Re_{VV} = \frac{\epsilon\cos\theta - \sqrt{\epsilon - \sin^2\theta}}{\epsilon\cos\theta + \sqrt{\epsilon - \sin^2\theta}} \tag{2.30}$$

Recall that GPS signals are RHCP. When a circularly polarized wave reflects off a surface, a portion of the wave reverses polarization into a left hand circularly polarized (LHCP) wave. The two components are known as the co- and cross-polarizations, given by Equations 2.31 and 2.32:

$$\Re_{co} = (\Re_{VV} + \Re_{HH})/2 \tag{2.31}$$

$$\Re_{cross} = (\Re_{VV} - \Re_{HH})/2 \tag{2.32}$$

There is an angle of incidence where the dominant polarization shifts from cross-polarization to co-polarization. This angle is known as Brewster's angle, defined as:

$$\theta_B = \arctan(n_2/n_1) \tag{2.33}$$

For incidence angles less than Brewster's angle, most of the reflected GPS signal is LHCP. For angles greater than Brewster's angle, the RHCP component increases significantly. For this reason, the nadir antenna used in GNSS-R should be LHCP. This is also significant because the opposite polarization helps reject unwanted RHCP components that are detected, and defines a filter for visible satellites with large incidence angles.

Once the Fresnel reflection coefficient is determined, the dielectric constant can then be estimated. However, inverting Equations 2.29 and 2.30 to solve for ϵ is difficult. To estimate the dielectric constant, an iterative approach is used. The estimate is adjusted until the Fresnel reflection coefficient converges to the value calculated from the KAGO model.

2.9 An Alternative Method

Current GNSS-R methods involve sampling raw GPS signals and processing them into delay waveforms and delay-Doppler maps (DDMs). A delay waveform is the signal power as a function of the delay. An example of a delay waveform is shown in Figure 2.5. A DDM is composed of multiple delay waveforms as a function of frequency. An example of a simulated DDM is shown in Figure 2.6. DDMs show the spreading of the reflecting signal over the glistening zone at a particular time. The shape of the DDM represents the roughness of the reflecting area. This is useful for GNSS-R applications such as ocean wind speeds; however, it is not useful for remote sensing of sea ice and land. Furthermore, DDMs are difficult to interpret without a working knowledge of GNSS-R.

The purpose of introducing an alternative method is to simplify GNSS-R to be compatible with a CubeSat platform, limited by processing power and downlink bandwidth. This method attempts to identify different types of sea ice by estimating the dielectric constant through the BRCS. There are four parameters required for this method:

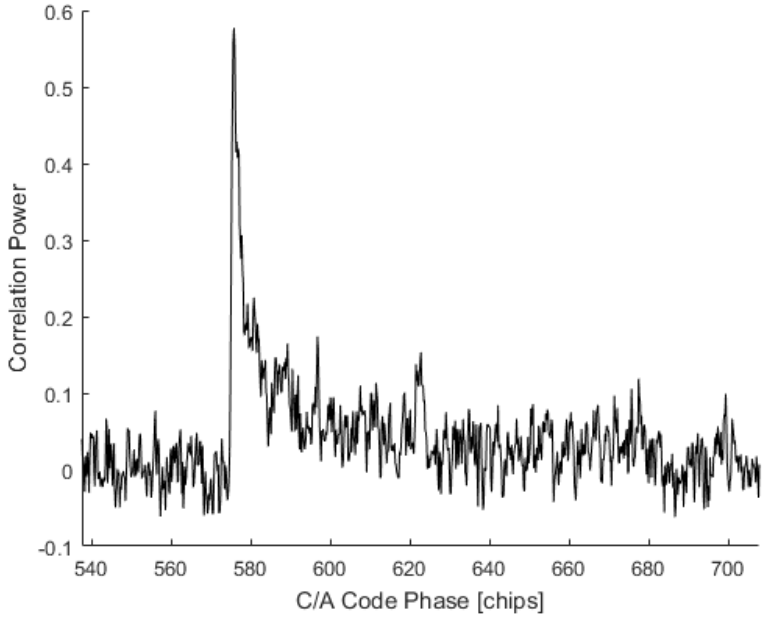

Figure 2.5: Example of a Delay Waveform

1. GPS Time
2. PRN
3. Pseudorange
4. SNR or C/N_0

The first three items is acquired using the direct signal, while the last item must be acquired from both signals. The GPS time is needed to set the measurements and determine the locations of the GPS satellites, identified by the PRN. The pseudorange is an estimate of the distance between the transmitting satellite and the receiver. This is estimated by timing the signal and multiplying by the speed of light, and can be improved in accuracy by incorporating the phase of the signal. Depending on the complexity of the design and ITAR compliance, the pseudorange can be replaced with position data. Finally, the SNR or C/N_0 is the actual measurement required for the alternative method. From here, the data processing for estimating dielectric constants can be accomplished using the methods and algorithms described in this Chapter. It is also notable that the alternative method can be used to process all visible satellites, whereas DDMs are restricted to a single satellite.

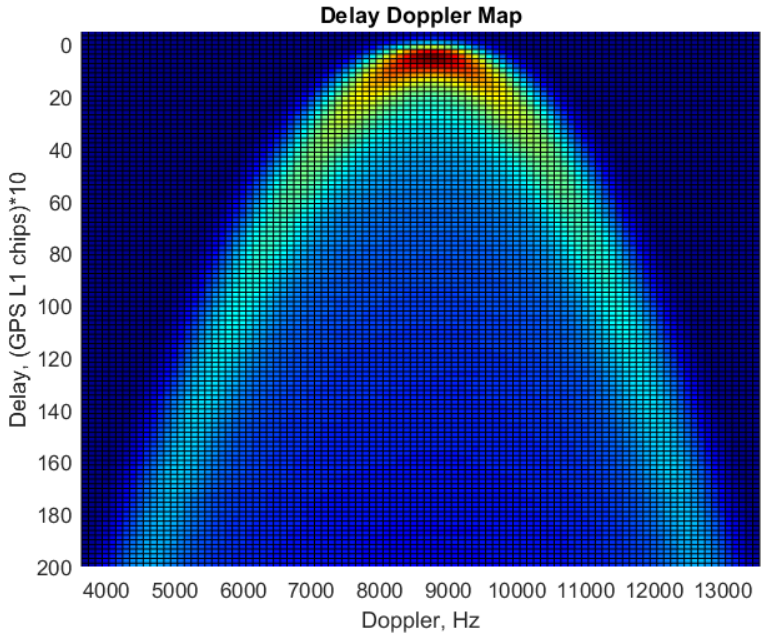

Figure 2.6: Example of a Delay-Doppler Map

Chapter 3

Processing with UK-DMC Data

3.1 Introduction

The Disaster Monitoring Constellation (DMC) is a remote sensing collaboration between Algeria, China, Nigeria, Turkey, and the United Kingdom. The purpose of the DMC is to provide Earth imagery for disaster relief. The first UK-DMC satellite was launched in 2003 and carried several secondary payloads, including a GNSS-R experiment payload. The satellite operates in a sun-synchronous low Earth orbit (LEO) approximately 680 km above the Earth. A custom left-hand circularly polarized antenna with peak gain of 11.8 dBiC was designed for the GNSS-R experiment. The GPS receiver was designed by Surrey Satellite Technology Limited (SSTL) and is based on Zarlink's front-end receiver and correlator [25]. The GNSS signals are downconverted from L1 to 4.309 MHz intermediate frequency (IF) and sampled at 5.714 MHz using 2 bits (sign and magnitude), resulting in IF samples centred on 1.405 MHz. The data recorder is capable of logging 20 seconds of continuous data [25].

The purpose of re-processing the UK-DMC data is to verify the new method for GNSS-R outlined in the previous chapter. The UK-DMC data has been discussed extensively in [25] and provide a baseline for the expected results of the alternative method. However, the dielectric values are not covered in [25] and must be based off other literature, such as the values provided in Table 2.2.

3.2 Data Sets

Three raw data files recorded by the UK-DMC satellite are publicly available through Gleason's PhD dissertation [25] and book [34]. The details of these data files are summarized in

Table 3.1: UK-DMC Data Sets

Data	Date	Time	Region	PRN(s)
Ocean	Nov. 16, 2004	07:54:37	NE Pacific	22
Ice	Feb. 4, 2005	10:24:03	Alaska	13
Land	Dec. 7, 2005	05:03:12	Nebraska	15, 18

Table 3.1. The data files also come with a software program called Daaxa, which is designed to process the raw data. The details for the software program can be found in Gleason's PhD dissertation [25]. The raw data was processed with Daaxa using an incoherent integration time of one second. This produces an output file for each second of data in the raw data file, containing the signal power for a specified Doppler range and a chip delay range. These outputs can then be imported into MATLAB to create delay waveforms and DDMs.

For the alternative method, the GPS time, PRN, and receiver location are provided. However, the Daaxa software outputs the power while iterating through Doppler and delay. This is not compatible with the proposed method and needs to be converted into SNR. The SNR is estimated using the second method discussed in Chapter 2.

3.3 Results

The results presented in this section are obtained using 100 ms of averaging in the Daaxa software. All other processing is performed in MATLAB using the steps described in Chapter 5. The scattering area used is the isorange ellipse divided by three.

Figures 3.1 and 3.2 show the results for the ocean data. The mss is reported as 0.0075 according to data from the National Data Buoy Centre [25].

Figures 3.3 and 3.4 show the results for the ice data. The mss is estimated to be 0.00003. This value is purely a guess based on the knowledge that the ice present is thin first year ice 30-70 cm thick, is likely more flat than the mss estimates for land, and is not considered rough due to a significant coherent component of the reflected signal.

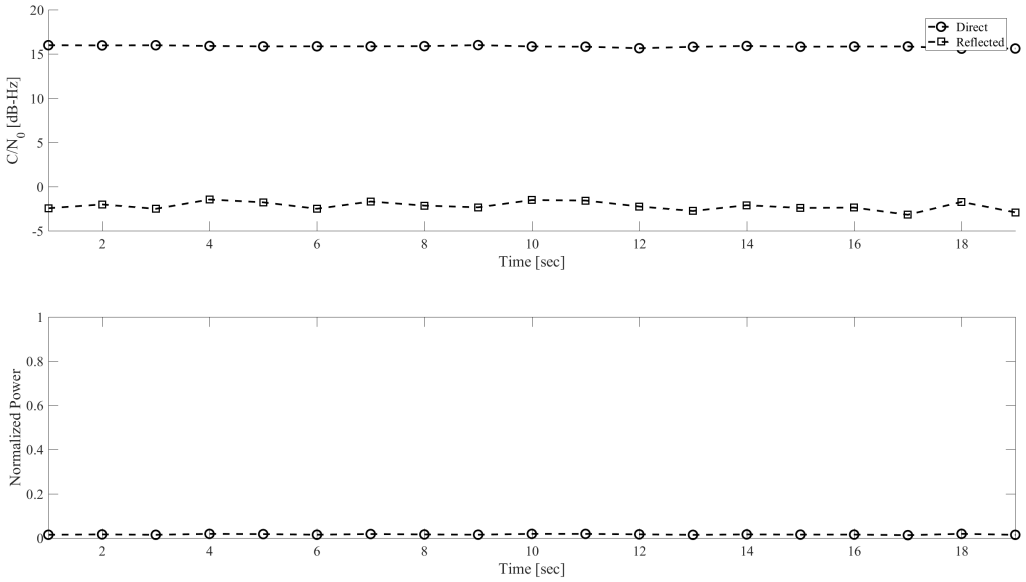

Figure 3.1: Power for UK-DMC Ocean Data

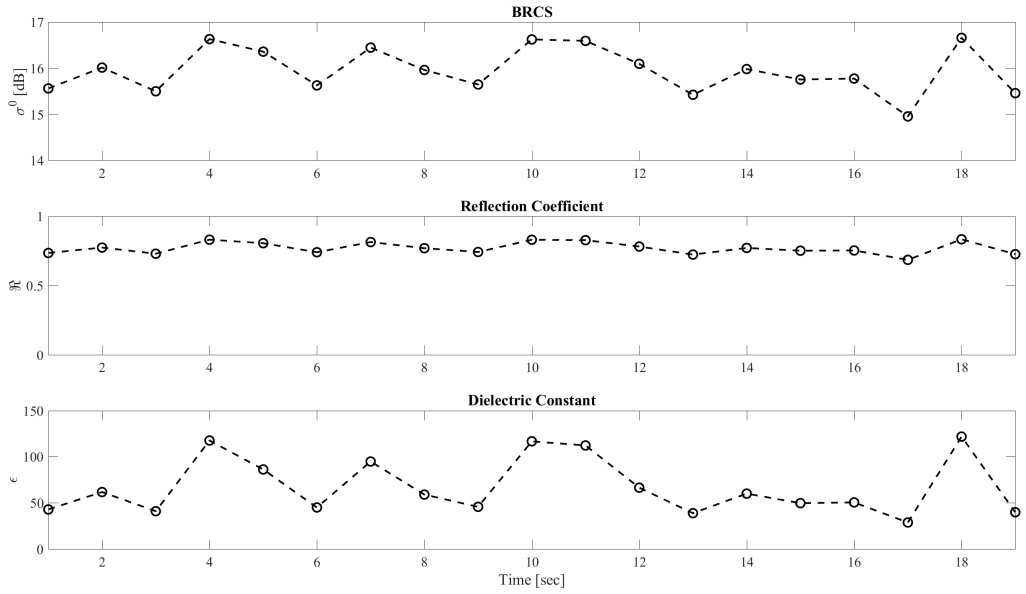

Figure 3.2: Dielectric for UK-DMC Ocean Data

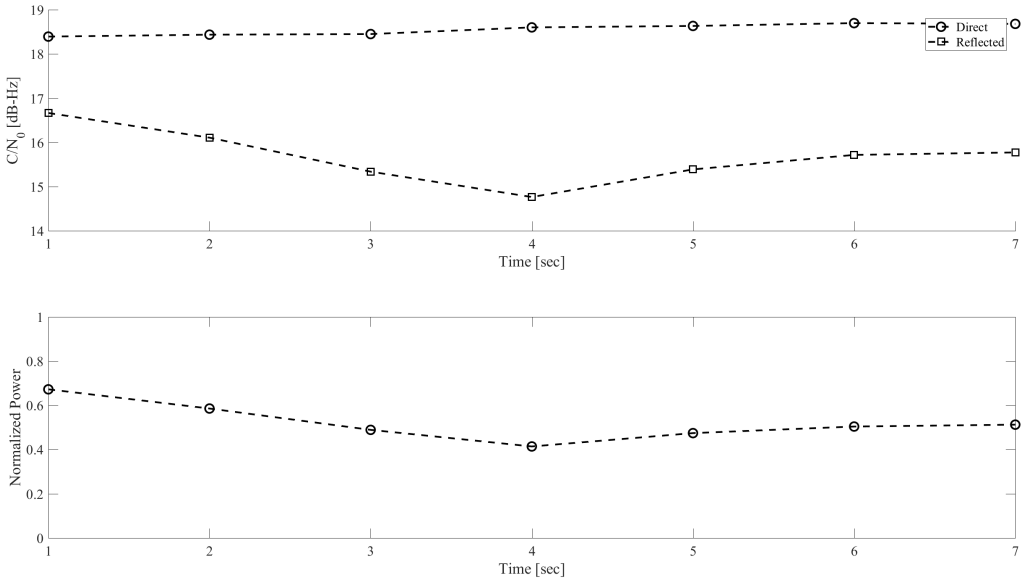

Figure 3.3: Power for UK-DMC Ice Data

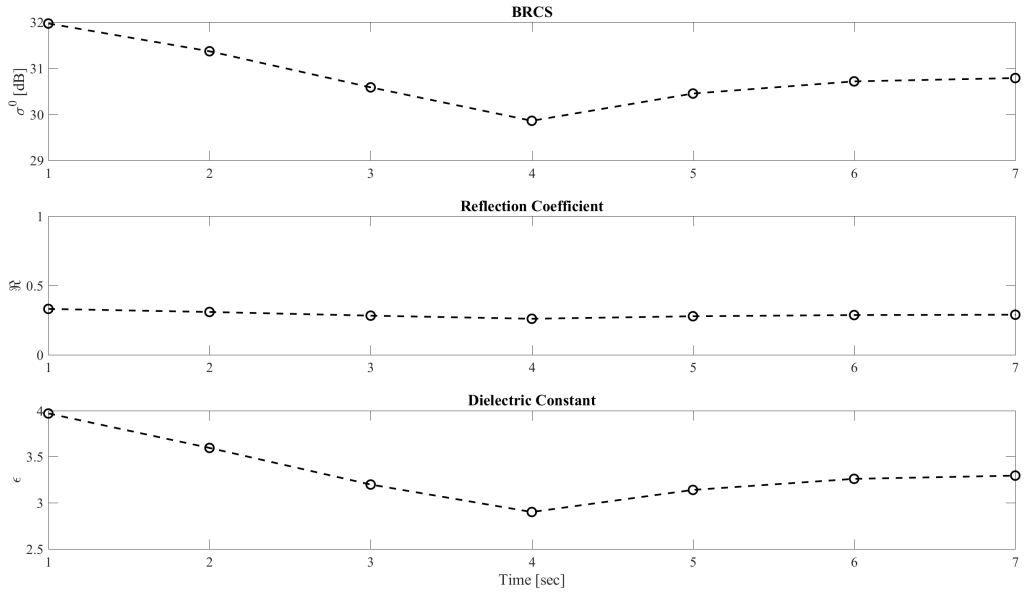

Figure 3.4: Dielectric for UK-DMC Ice Data

Figure 3.5 shows the location of the UK-DMC land data. Omaha, Nebraska is located to the east of PRN 18, with the Missouri River east of Omaha and crosses the specular path in the first seconds. PRN 18 also crosses the Platte River in the last seconds of data collection. Lincoln, Nebraska is located to the west of PRN 15 near the first couple seconds of data collection, and Beatrice, Nebraska around second 10. Figures 3.6-3.9 show the results for the land data. The *mss* is estimated using the elevation profiles along the specular points pulled from Google Earth. The *mss* values used are 0.0004 and 0.0006 for PRNs 15 and 18 respectively. The elevation and variance are shown in Figures 3.10-3.13.

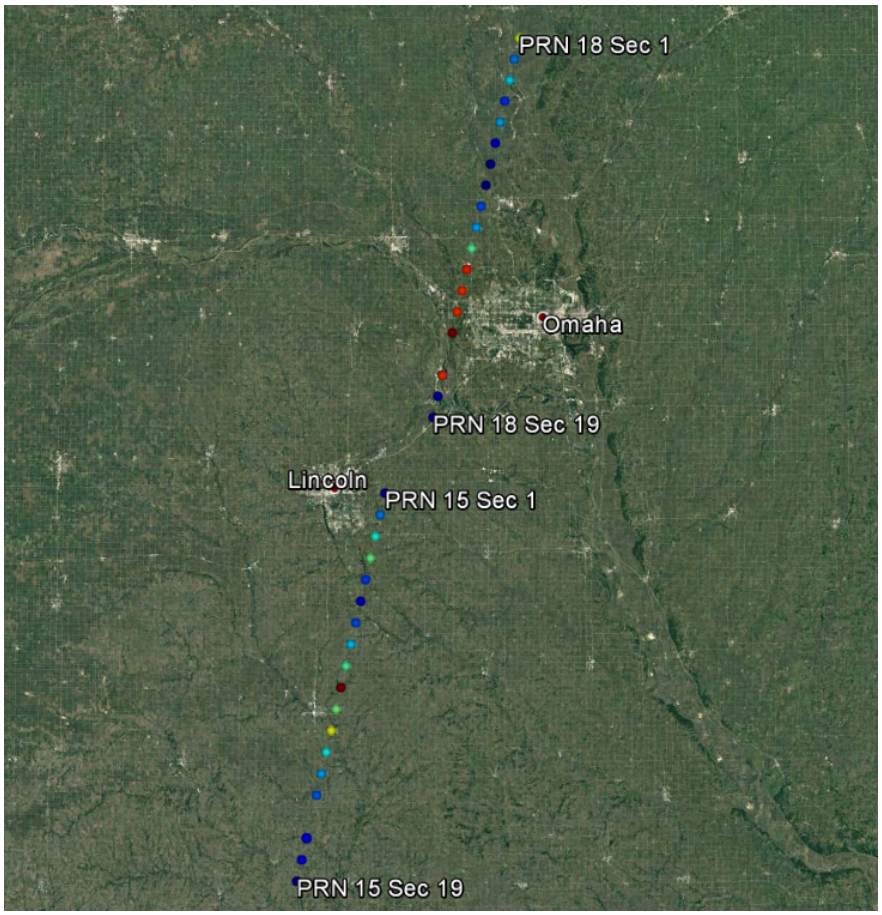

Figure 3.5: Google Earth Image of UK-DMC Land Data Collection Area

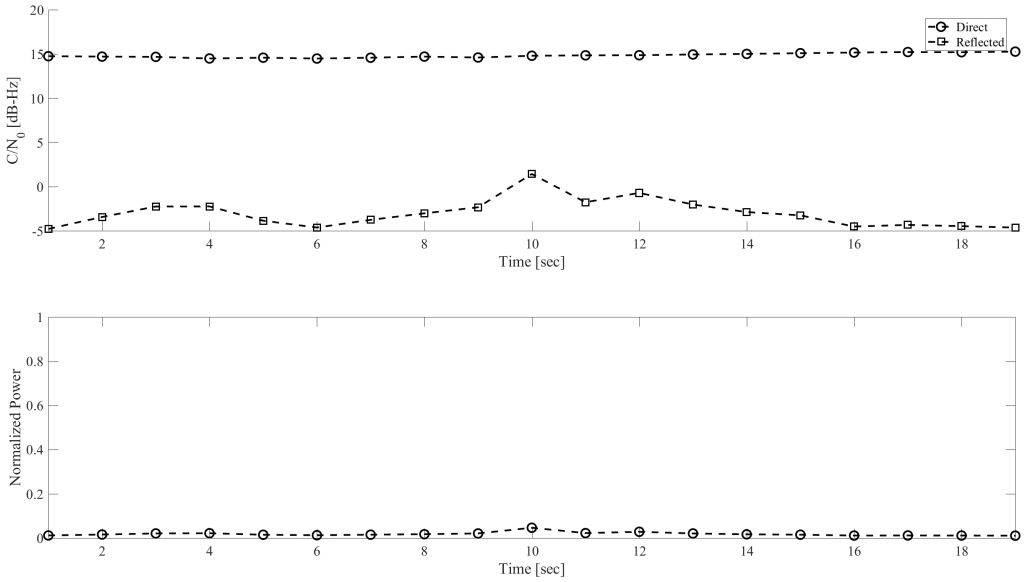

Figure 3.6: Power for UK-DMC Land PRN 15 Data

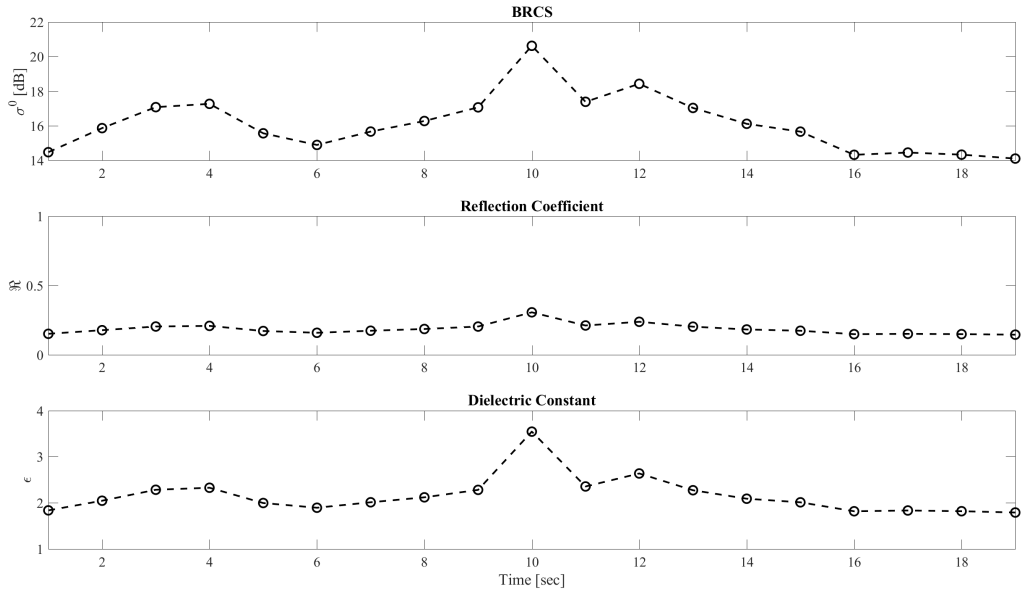

Figure 3.7: Dielectric for UK-DMC Land PRN 15 Data

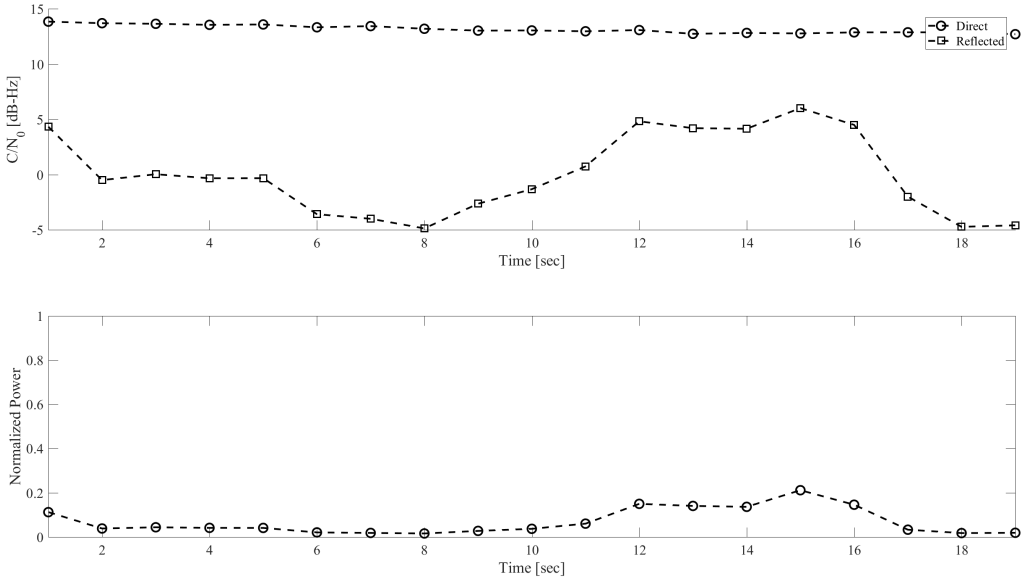

Figure 3.8: Power for UK-DMC Land PRN 18 Data

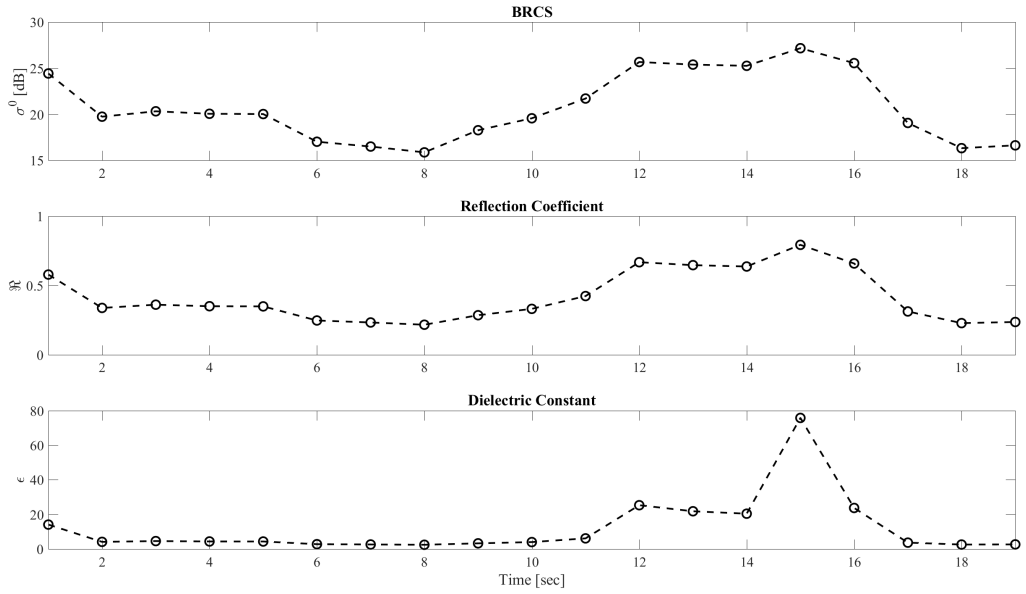

Figure 3.9: Dielectric for UK-DMC Land PRN 18 Data

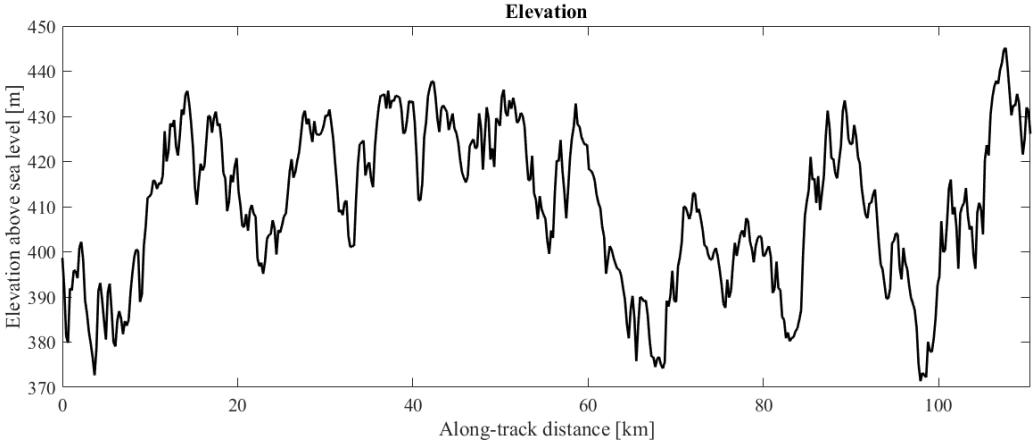

Figure 3.10: Elevation Profile for UK-DMC Land PRN 15 Data

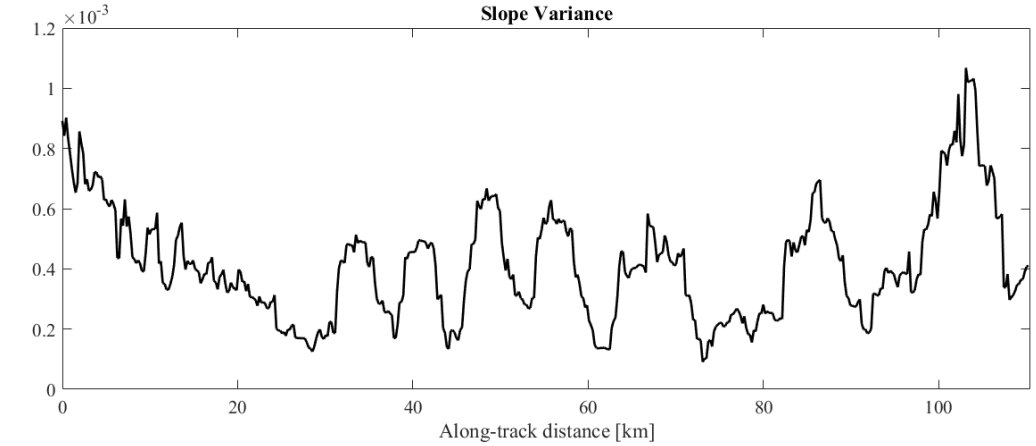

Figure 3.11: Elevation Variance for UK-DMC Land PRN 15 Data

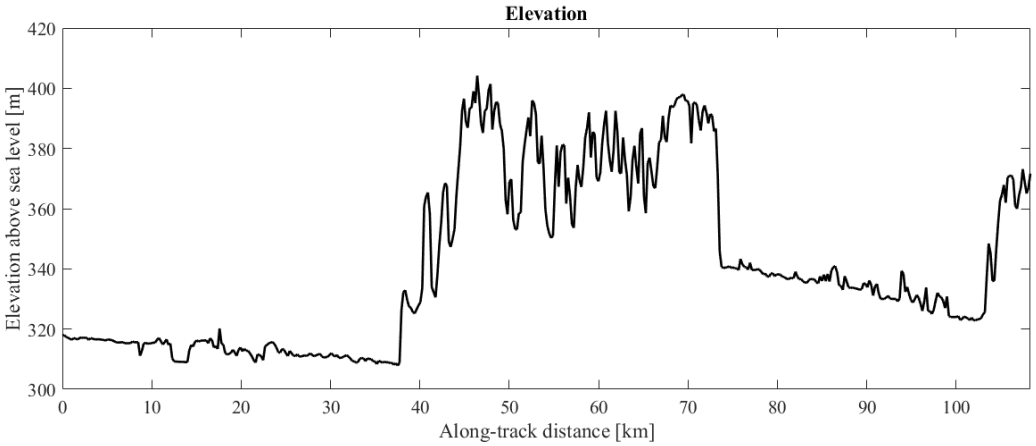

Figure 3.12: Elevation Profile for UK-DMC Land PRN 18 Data

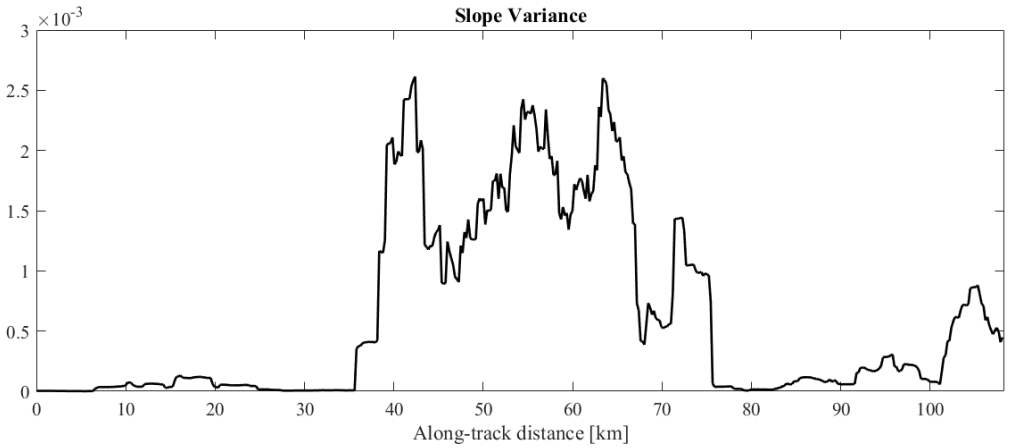

Figure 3.13: Elevation Variance for UK-DMC Land PRN 18 Data

The results presented show that the estimated dielectric constants are near the expected ranges, but can be very sensitive to the input mss value and scattering area. The results for the ocean and ice data remain rather stable, while the results for land follow the expected trends presented in [25]. The mss values used for processing the land data are constant across the entire specular path; however, the final results are likely more accurate with a variable mss value, especially for PRN 18. Nonetheless, the results from re-processing the UK-DMC data has served its purpose in validating the proposed method.

Chapter 4

Quadcopter Experiments

4.1 Hardware Design

Several GPS receivers were considered for the design of the GNSS-R payload on a CubeSat. The details for each GPS receiver is outlined in Table 4.1. Based on cost, availability, and ease of use and integration, the Jupiter SE868 v2 by Telit was selected for the design.

The SE868 is a positioning module that combines GPS and GLONASS to provide high performance navigation solutions in a small package. The module provides GNSS information over a serial interface using either the NMEA-0183 standard or SiRF OSP binary protocol. For the experiment, the SE868 is hard configured to turn on automatically on power-up and use UART as the serial interface. Furthermore, the SE868 is configured to use the SiRF protocol via software. The SE868 operates using 1.8 volts.

The antennas used in the experiment are a Linx SH series for the direct RHCP signals and an Antcom 1G1215A for the reflected LHCP signals. Both are active antennas that have a built-in low noise amplifier (LNA), which are powered using a bias-T at 3.3 volts. The

Table 4.1: GPS Receivers

Model	Manufacturer	Data Format
GNS 2201	GNS Electronics	NMEA-0183/Binary
A5100-A	Maestro Wireless	NMEA-0183/Binary
OEM615	NovAtel	NMEA-0183/Binary
SdrNav00	OneTalent GNSS	Raw IF
GN3S v3	University of Colorado/SiGe	Raw IF
SGR-05U	SSTL	Binary
SE868 v2	Telit	NMEA-0183/Binary
SE41x0L	SiGe	Raw IF

RHCP antenna has a gain of 5 dB and the LHCP antenna has a gain of 3 dB.

Serial communication is established using a USB-to-UART interface. Power is also provided to the SE868, LNAs, and USB-to-UART via USB. Two voltage converters provide the 3.3 and 1.8 volts needed for all the components. The initial design called for USB as the interface protocol since it is simple to implement; however, the low data rate is not ideal and will be replaced in subsequent designs.

A custom printed circuit board (PCB) was designed to hold the GPS receivers and communication interface. The circuit for the direct GPS receiver is identical to the circuit for the reflected GPS receiver. The PCB was designed to be included in WatSat's CubeSat design. WatSat's design called for PCBs to be stacked using standoffs in each corner, with headers on two opposing edges and cutouts on the remaining two edges for the GPS antennas. The connectors for the antennas are positioned such that the antennas will have a direct connection when assembled on the CubeSat. The USB output is routed to both the headers and separate USB ports for direct connections. The PCB layout is shown in Figure 4.1.

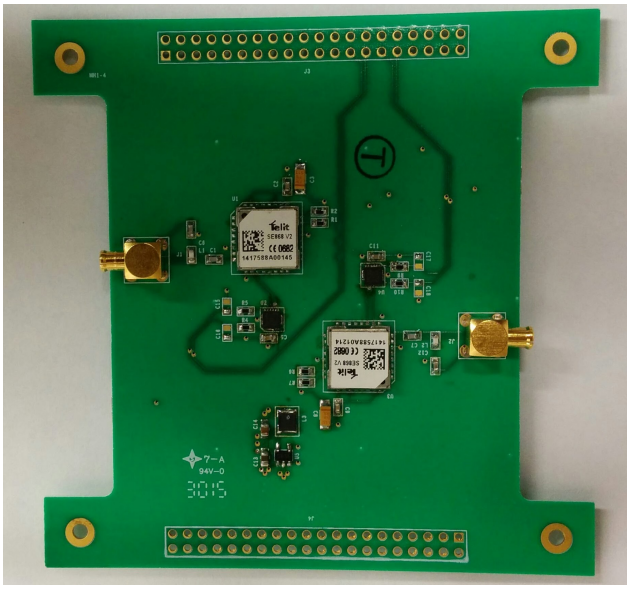

Figure 4.1: Custom PCB Design for GNSS-R on CubeSat

4.2 Quadcopter Setup

The first flight test was performed with the help of the WAVELab, directed by Professor Steven Waslander at the University of Waterloo. The GNSS-R payload was attached to a custom quadcopter equipped with a Hardkernel ODROID XU4 single-board computer and

a Pixhawk Autopilot flight controller. The purpose of this flight was to test the payload design and to ensure that the components were operating as expected.

After the first flight, the payload was moved to a different quadcopter, a DJI Flamewheel F450. The purpose of this is to provide experimental data for processing using the alternative method. This quadcopter is equipped with a Raspberry Pi 3 Model B and a DJI Naza-M Lite flight controller. The flight controller was upgraded with the Naza-M V2 firmware for better performance. The quadcopter is powered using a Turnigy 5000 mAh 3S 25C lithium polymer battery. In order to power the Raspberry Pi and the GNSS-R PCB using the quadcopter battery, a Murata OKL-T/6-W12 power converter is included. The full setup is shown in Figure 4.2.

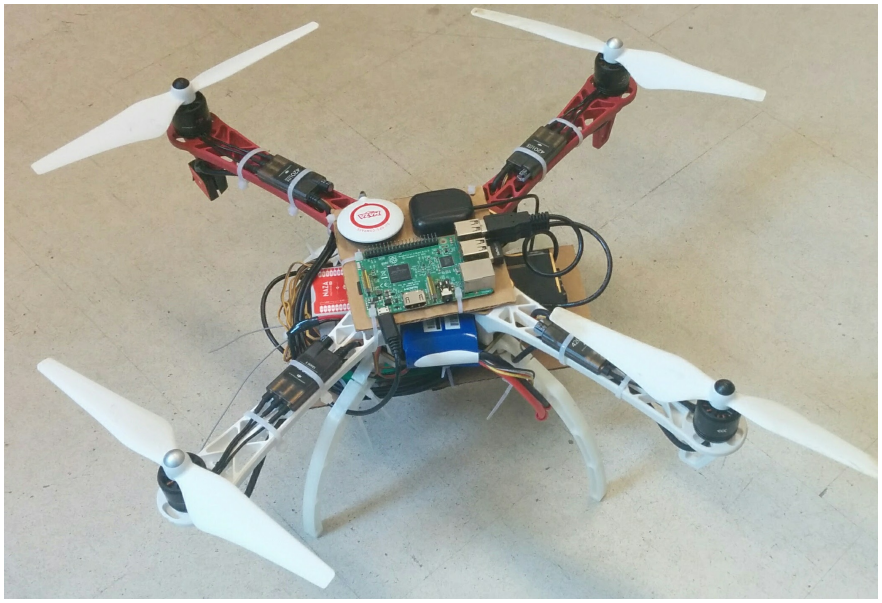

Figure 4.2: Quadcopter Setup

A Python script was written for recording the data. The script configures the SE868 to output using SiRF protocol and alternates writing bytes from both receivers into two separate files, named using the date, time, and port. The recording time is passed into the script as an argument. After the outputs are written to their respective files, each SiRF message is identified and broken into separate lines. The script is executed remotely on the Raspberry Pi using a VNC connection to a laptop.

4.3 Quadcopter Flights

Table 4.2 summarizes the flights where data was recorded. Flights were conducted on two sides of Columbia Lake just north of the University of Waterloo, shown in Figures 4.3 and 4.4. The eastern shore has a picnic area between two playing fields. At the edges of these fields are several trees and the ground slopes down to the picnic area. There is also a gravel walking path stretching along the eastern shore of the lake, with a small shed by the shore. The eastern side of the lake also contains an island located just off the shore by the shed and picnic area. The western side of the flight area is located on an island, with a few trees located to the south and the northwest. The University of Waterloo's weather station is located at the south end of the island. This area is much flatter than the east side and has a better view of the lake; however, the area is more difficult to access by foot.

Table 4.2: Quadcopter Flights

Set	Date	UTC Time	Coordinates	Altitude [m]
1	Oct. 10, 2016	20:58	43.4751, -80.5507	359
2	Oct. 12, 2016	18:27	43.4740, -80.5532	347
3	Oct. 12, 2016	18:30	43.4740, -80.5532	350
4	Oct. 26, 2016	18:09	43.4740, -80.5532	346
5	Oct. 26, 2016	18:23	43.4740, -80.5534	357
6	Nov. 15, 2016	17:28	43.4741, -80.5567	358
7	Jun. 7, 2017	19:42	43.4738, -80.5531	335
8	Jun. 8, 2017	19:37	43.4739, -80.5533	342
9	Jun. 16, 2017	15:07	43.4741, -80.5565	359

Figure 4.3: Columbia Lake East

Figure 4.4: Columbia Lake West

Chapter 5

Experiment Results

5.1 Post-Processing Data Files

Data recorded during quadcopter flights produce two files, one for each GPS receiver. Each line in these files contain SiRF messages, which needs to be interpreted. There are several messages of interest, listed in Table 5.1. The SiRF message structure is shown in Table 5.2. Each message ID varies in length depending on the information included in that message. A Python script is used to parse the SiRF message files by message ID and outputs the data into CSV files. The data in the CSV files can then be imported into MATLAB.

Table 5.1: SiRF Messages

Message ID	Name
02 (0x02)	Measured Navigation Data
07 (0x07)	Clock Status Data
13 (0x0D)	Visible List
28 (0x1C)	Navigation Library Measurement Data
30 (0x1E)	Navigation Library SV State Data
41 (0x29)	Geodetic Navigation Data

Table 5.2: SiRF Message Structure

Start Sequence	Payload Length	Payload	Message Checksum	End Sequence
0xA0A2	2 bytes (15 bits)	Up to 1023	2 bytes (15 bits)	0xB0B3

The use of USB and Raspberry Pi for recording data is slow compared to the amount of data generated from the GPS receivers. This caused messages to be lost occasionally, likely due to the data buffer overflowing. To mitigate this, the first step in MATLAB processing

is arrange the data by GPS time and interpolate any missing data. This step also retrieves the GPS time, which is then used to download the appropriate IGS file and.

The next step calculates the locations of the visible GPS satellites using the orbit interpolation algorithm described in Chapter 2. The quadcopter location is then calculated using the least squares method. Here the clock correction data from the GPS receivers are applied to the pseudoranges before the receiver location is calculated. However, because the position data is available from the GPS receivers, the position data was used instead of the calculated values in order to improve the accuracy of the results.

Once the locations of the transmitters and receiver are determined, the location of the specular points can then be calculated using the algorithm described in Chapter 2. The scattering area is estimated and the BRCS is estimated, again using the equations described in Chapter 2. From there, the Fresnel reflection coefficient and the dielectric constant is estimated. In order to show the results in Google Earth, the results are incorporated into a KML file.

5.2 Comparing Dielectrics to Google Earth

In this section, the results for each data set are presented. The results include a table of visible satellites and their locations, a Google Earth overlay showing the specular locations and approximate scattering area, and two MATLAB plots for normalized power and dielectric constants. Each PRN is given a label for comparison between the Google Earth map and the MATLAB plots. The maps show a pin for the location of the quadcopter and receivers, and circular areas for the glistening zones. As mentioned in Chapter 2, the glistening zones are elliptical and increase in eccentricity as the incidence angle increases. This is either very difficult or impossible to automate for Google Earth overlays; however, the circles shown are accurate in area size.

5.2.1 Data Set 1

Table 5.3 and Figure 5.1 shows the location of the specular points and the glistening zones for each GPS satellite in view. Figure 5.2 shows the power and Figure 5.3 shows the estimated dielectric constant for each satellite. In the first data set, the power received does not remain stable throughout the data collection for PRNs 15, 18, and 20 (labels C, D, and E). The fluctuations for PRN 18 could be caused by trees in the path, while PRNs 15 and 20 are likely caused by loss of signal.

Table 5.3: Data Set 1

Label	PRN	Azimuth	Incidence	Terrain
A	5	77.44	67.36	Land
B	13	59.07	36.99	Land
C	15	128.98	10.74	Land
D	18	277.92	51.85	Land
E	20	35.27	15.96	Land
F	21	301.88	27.68	Land
G	24	154.43	75.88	Land

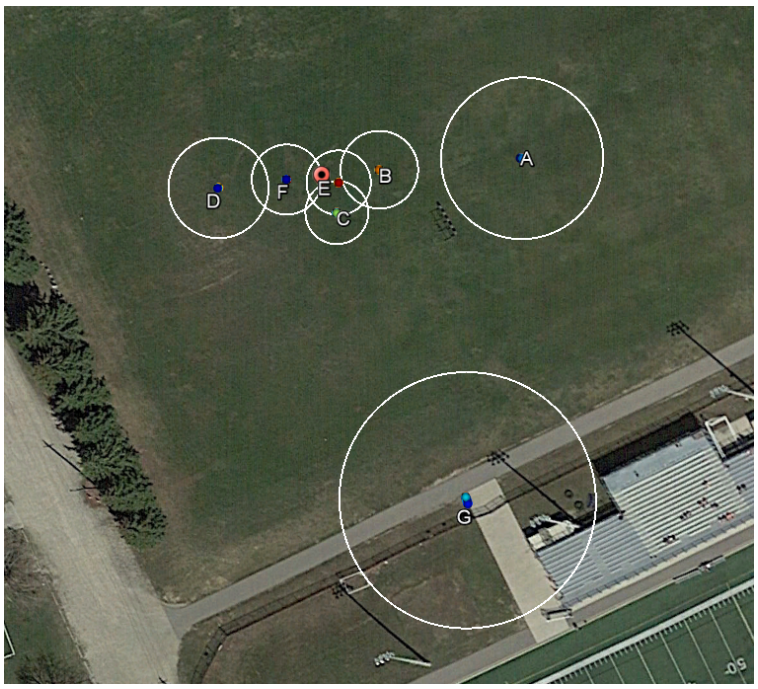

Figure 5.1: Data Set 1 Specular Locations

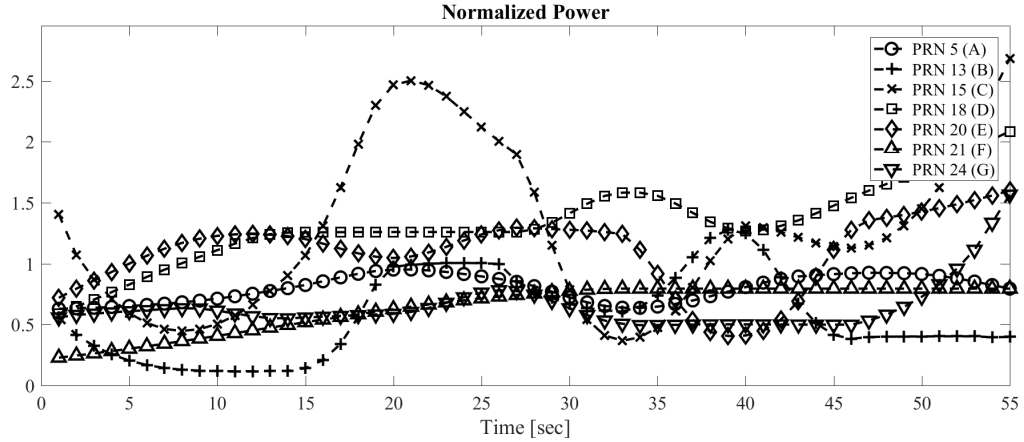

Figure 5.2: Data Set 1 Normalized Power

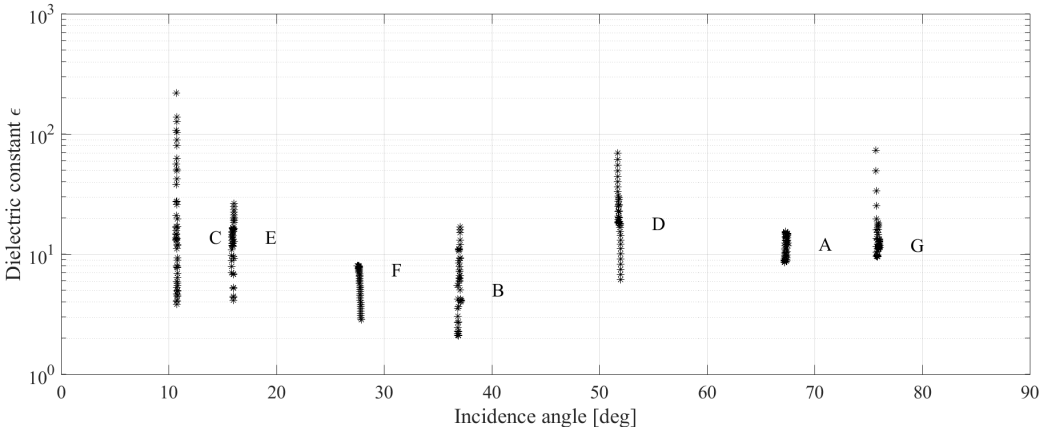

Figure 5.3: Data Set 1 Dielectrics

5.2.2 Data Set 2

Table 5.4 and Figure 5.4 show the locations for the second data set. The power and dielectrics are shown in Figures 5.5 and 5.6 respectively. In this data set, PRN 29 (label H) has a higher power received than the other specular points on land. This could be due to higher moisture content in the soil. Also noticeable is the lower power received from PRN 4 (label B). This could be due to the trees in the path or the slope of the reflecting area.

Table 5.4: Data Set 2

Label	PRN	Azimuth	Incidence	Terrain
A	2	91.69	40.19	Land
B	4	131.01	48.45	Land
C	5	37.24	9.46	Land
D	6	99.84	77.62	Land
E	15	186.12	75.10	Land
F	20	244.75	50.51	Land
G	25	247.57	71.32	Water
H	29	299.38	35.32	Land

Figure 5.4: Data Set 2 Specular Locations

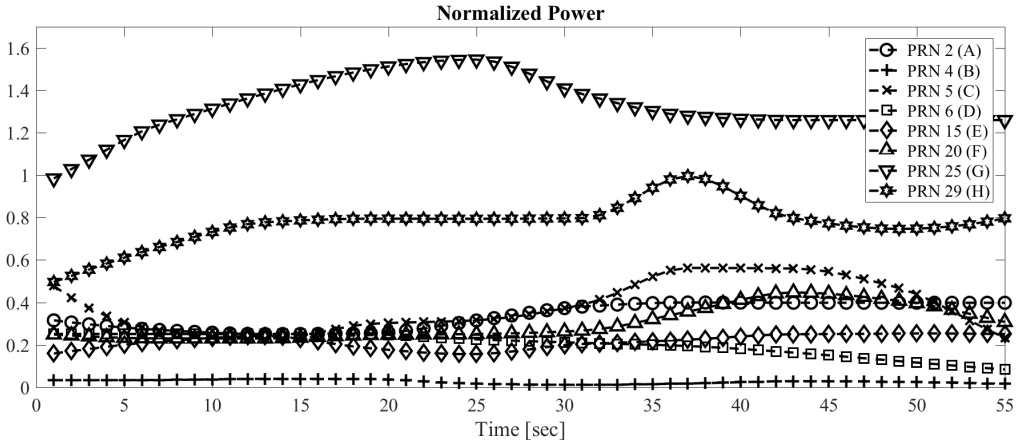

Figure 5.5: Data Set 2 Normalized Power

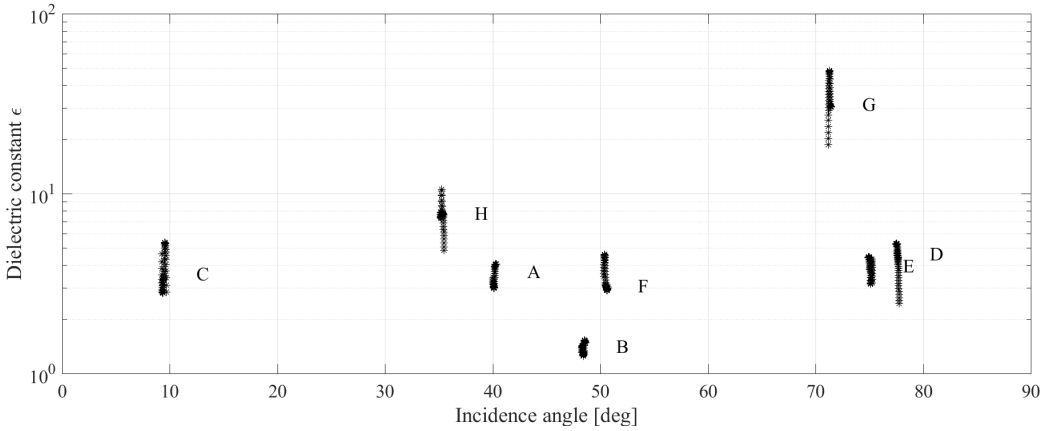

Figure 5.6: Data Set 2 Dielectrics

5.2.3 Data Set 3

Table 5.5 and Figure 5.7 show the locations for data set 3. Figures 5.8 and 5.9 show the power and dielectric constants. This data set shows the best distinction between water and land.

Table 5.5: Data Set 3

Label	PRN	Azimuth	Incidence	Terrain
A	2	93.29	41.46	Land
B	4	129.40	47.19	Land
C	5	38.58	11.12	Land
D	6	100.88	78.75	Land
E	15	185.93	73.62	Land
F	20	245.93	49.12	Land
G	21	290.29	79.56	Water
H	25	246.33	71.32	Water

Figure 5.7: Data Set 3 Specular Locations

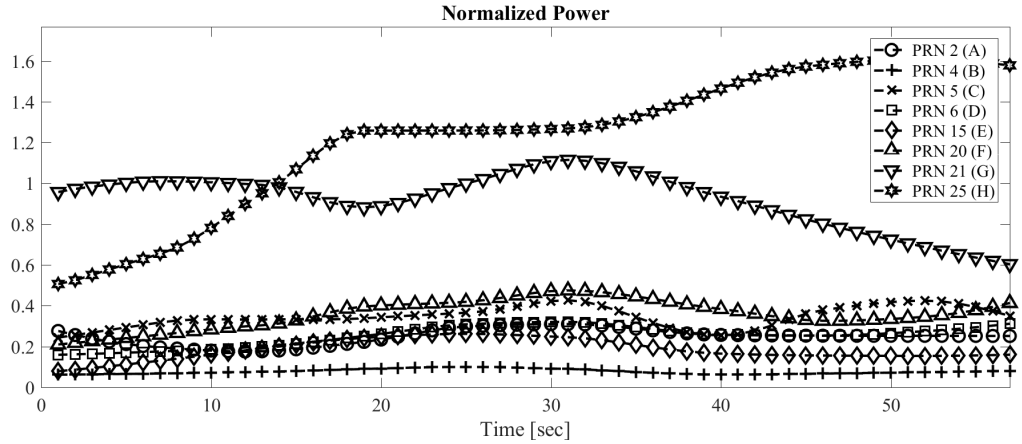

Figure 5.8: Data Set 3 Normalized Power

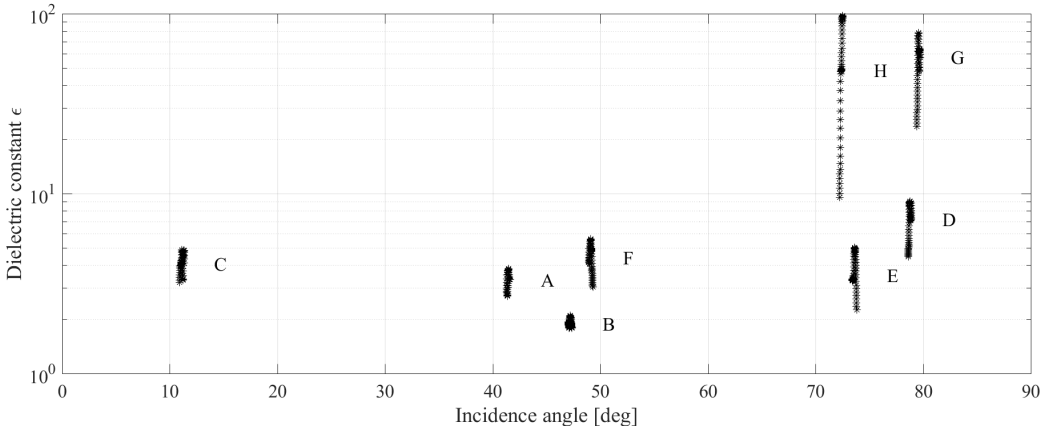

Figure 5.9: Data Set 3 Dielectrics

5.2.4 Data Set 4

Table 5.6 and Figures 5.10-5.12 show the results for data set 4. This data set also shows some power fluctuations, as well as PRN 21 (label G) occurring on both land and water. The fluctuations for PRNs 15, 20, and 29 (labels E, F, and H) are likely caused by terrain.

Table 5.6: Data Set 4

Label	PRN	Azimuth	Incidence	Terrain
A	2	107.60	55.02	Land
B	4	106.06	37.14	Land
C	5	49.24	28.06	Land
D	13	142.87	41.72	Land
E	15	184.42	57.38	Land
F	20	261.05	34.24	Land
G	21	297.81	68.30	Edge
H	29	266.97	27.09	Land

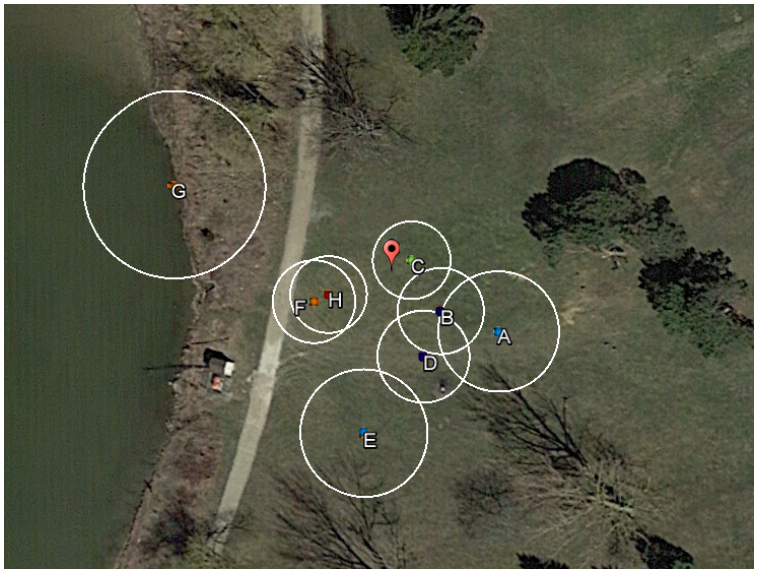

Figure 5.10: Data Set 4 Specular Locations

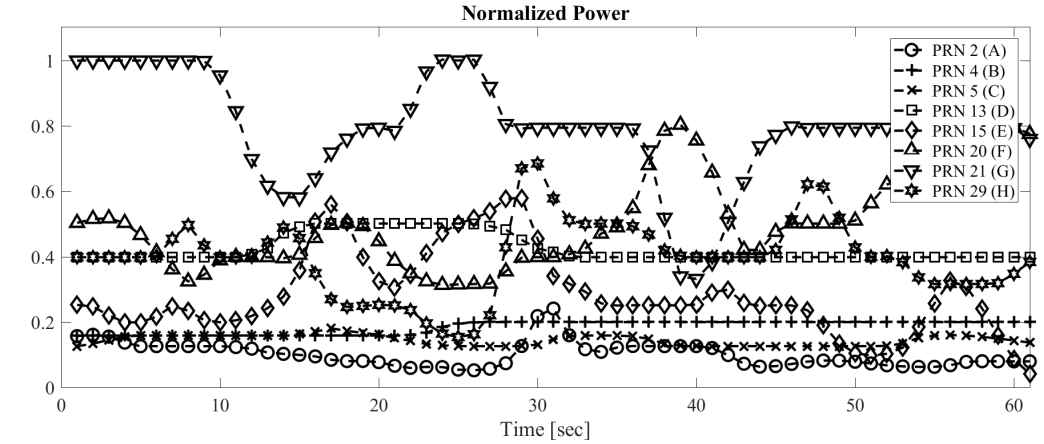

Figure 5.11: Data Set 4 Normalized Power

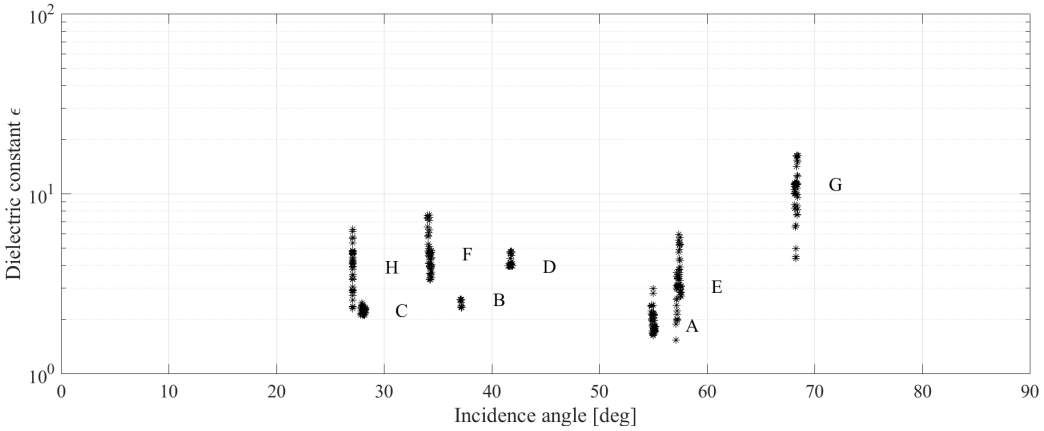

Figure 5.12: Data Set 4 Dielectrics

5.2.5 Data Set 5

Data set 5 is summarized in Table 5.7 and Figures 5.13-5.15. This data set shows the water specular points (PRN 21, label G) with a lower power ratio than other data sets. Also noticeable are the fluctuations for PRNs 4, 5, and 15 (labels B, C, and E). It is possible these measurements are influenced by the surrounding trees and slope of the ground.

Table 5.7: Data Set 5

Label	PRN	Azimuth	Incidence	Terrain
A	2	112.15	60.21	Land
B	4	94.95	35.66	Land
C	5	52.82	33.98	Land
D	13	135.95	36.31	Land
E	15	183.76	50.81	Land
F	20	268.70	28.99	Land
G	21	300.26	63.48	Water
H	29	252.09	27.77	Land

Figure 5.13: Data Set 5 Specular Locations

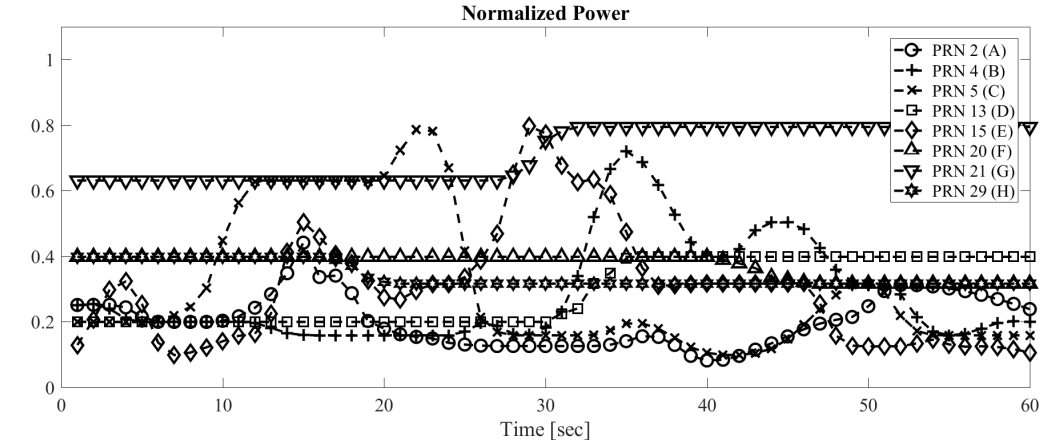

Figure 5.14: Data Set 5 Normalized Power

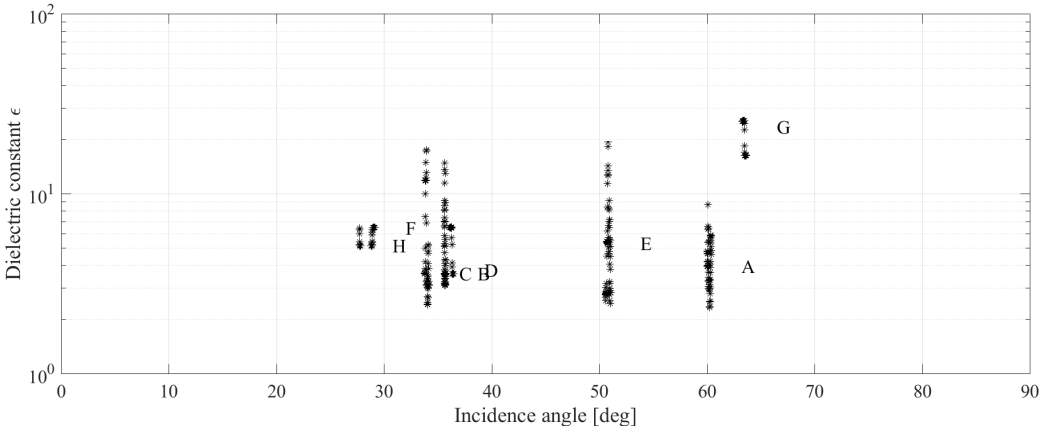

Figure 5.15: Data Set 5 Dielectrics

5.2.6 Data Set 6

Table 5.8 and Figures 5.16-5.18 summarize the results for data set 6. In this set, PRN 5 (label A) lies between water and land. PRNs 20 and 21 (labels D and E) also shows power fluctuations, again possibly caused by the trees in the path.

Table 5.8: Data Set 6

Label	PRN	Azimuth	Incidence	Terrain
A	5	60.40	45.70	Land
B	13	114.72	28.35	Land
C	15	181.69	37.42	Land
D	20	292.52	18.56	Land
E	21	304.09	54.39	Land
F	30	57.03	78.86	Water

Figure 5.16: Data Set 6 Specular Locations

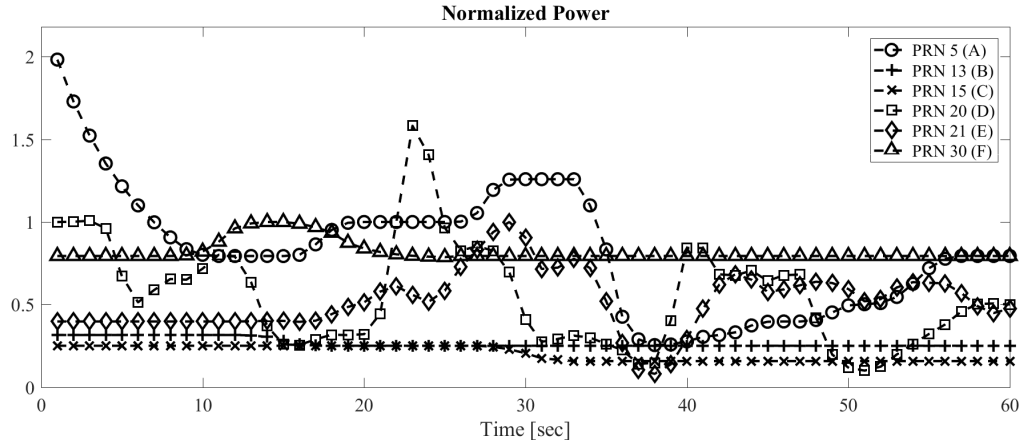

Figure 5.17: Data Set 6 Normalized Power

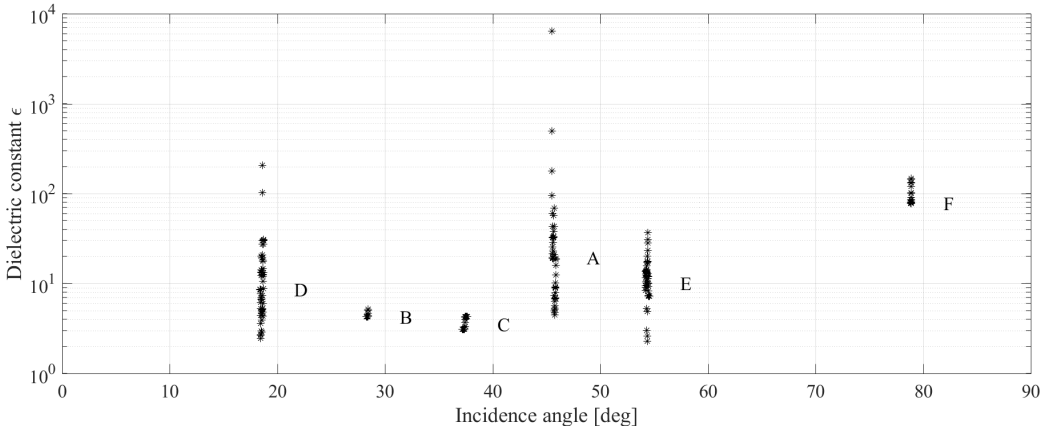

Figure 5.18: Data Set 6 Dielectrics

5.2.7 Data Set 7

For data set 7, the altitude for data collection was much lower than the other data sets. The large spikes in power ratio for PRN 3 (label B) could be caused by weak direct signals due to the scenery.

Table 5.9: Data Set 7

Label	PRN	Azimuth	Incidence	Terrain
A	1	64.36	37.05	Land
B	3	119.58	74.88	Land
C	11	56.00	52.02	Land
D	17	273.78	33.56	Land
E	19	258.96	57.32	Land
F	22	91.71	69.70	Land

Figure 5.19: Data Set 7 Specular Locations

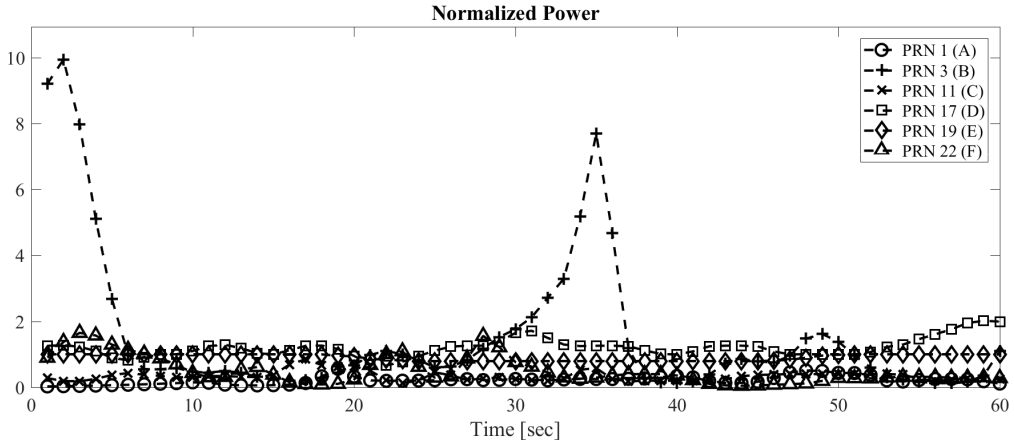

Figure 5.20: Data Set 7 Normalized Power

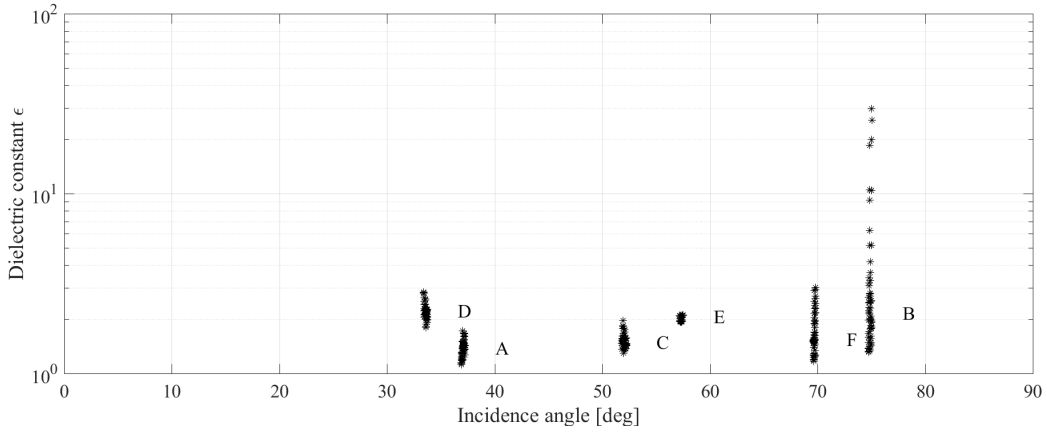

Figure 5.21: Data Set 7 Dielectrics

5.2.8 Data Set 8

The specular points for data set 8 happen to all occur over land, as shown in Figure 5.22. Figure 5.23 shows spikes in power for PRNs 11, 22, and 30 (labels D, G, and H). These could be caused by loss of signal due to trees in the way.

Table 5.10: Data Set 8

Label	PRN	Azimuth	Incidence	Terrain
A	1	65.26	36.55	Land
B	3	120.09	75.14	Land
C	7	172.30	79.92	Land
D	11	56.12	51.29	Land
E	17	272.87	34.09	Land
F	19	258.40	57.79	Land
G	22	92.40	69.83	Land
H	30	196.06	50.45	Land

Figure 5.22: Data Set 8 Specular Locations

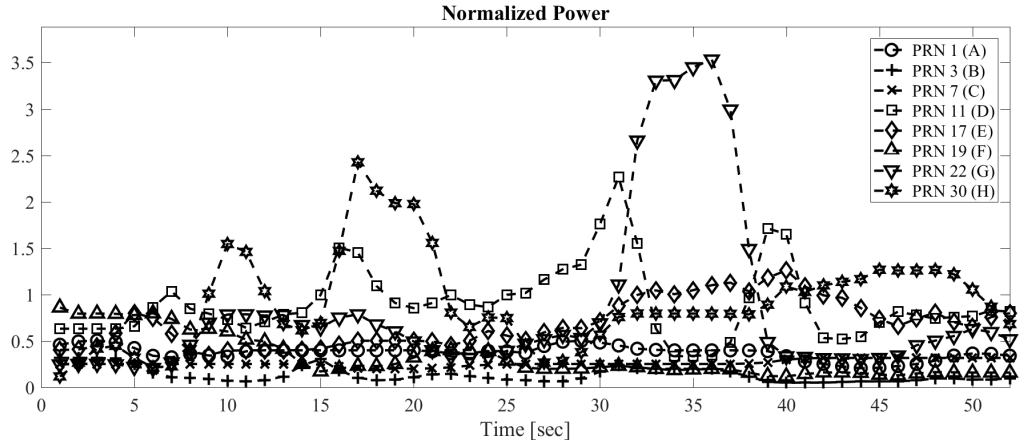

Figure 5.23: Data Set 8 Normalized Power

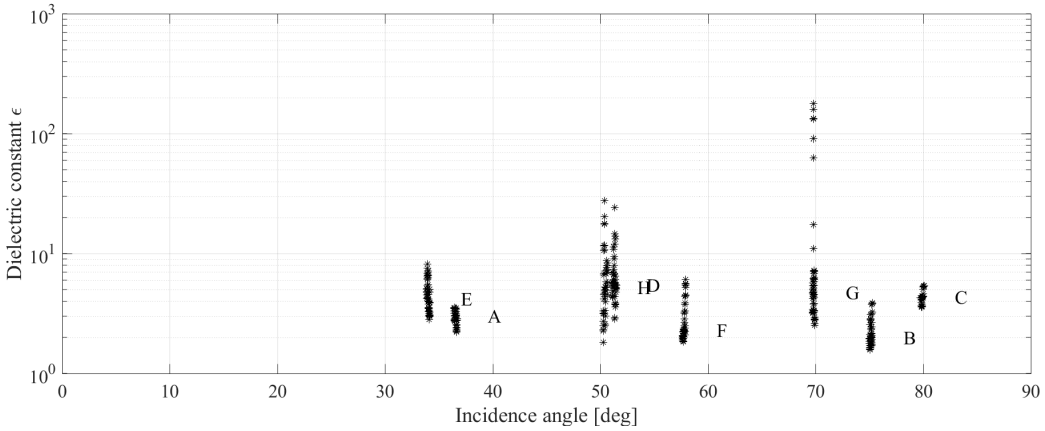

Figure 5.24: Data Set 8 Dielectrics

5.2.9 Data Set 9

Finally, Table 5.11 and Figures 5.25-5.27 show the results for data set 9. PRNs 16 and 27 (labels D and E) clearly shows water apart from land. PRNs 7 and 8 (labels A and B) show spikes in power, again possibly caused by temporary loss of GPS signal.

Table 5.11: Data Set 9

Label	PRN	Azimuth	Incidence	Terrain
A	7	308.69	38.72	Land
B	8	163.47	26.28	Land
C	9	241.60	40.09	Land
D	16	59.21	56.02	Water
E	27	72.72	30.06	Water
F	30	302.06	74.42	Land

Figure 5.25: Data Set 9 Specular Locations

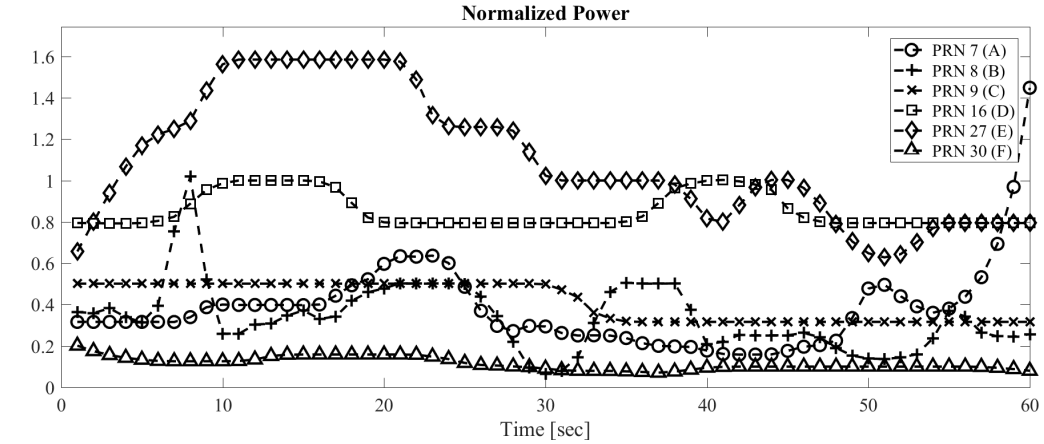

Figure 5.26: Data Set 9 Normalized Power

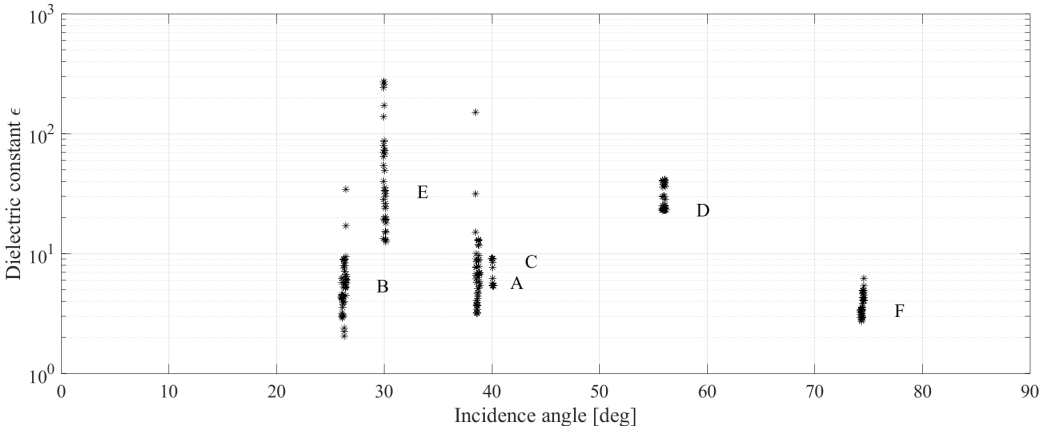

Figure 5.27: Data Set 9 Dielectrics

5.3 Sources of Error

Because of the fixed location of the quadcopter, the power is expected to be stable and contain only small fluctuations. The power is also expected to be higher for specular points over water than those over land. There are many factors that can cause the expected results to deviate. The analysis assumes that the quadcopter maintains a perfectly fixed position for the duration of each data collection period. However, this is highly unlikely and in reality the quadcopter drifts back and forth in all directions. It is possible that these drifts may have an effect on the sensitivity of the receiver tracking the reflected signals. Interference from both electromagnetic and physical sources is another possible source of error. Interference would cause weaker signals temporarily, possibly resulting in the power fluctuations seen. Finally, the uneven surfaces of the terrain around the test sites could also have an impact on the reflected power.

Chapter 6

Summary and Future Work

This thesis presents an alternative method for GNSS-R as a payload for a CubeSat. The size of CubeSats limit the amount of power available for on-board processing, and the amount of data generated by traditional GNSS-R exceeds the bandwidth available for data transmission. This method aims to reduce both the amount of processing and the amount of data generated.

To test the new method, a custom GNSS-R payload was designed and tested on a quadcopter platform. The GNSS-R payload was successfully able to detect the reflected GPS signals at Columbia Lake. Using the data recorded from the quadcopter, the specular locations and dielectric values were estimated and imported into Google Earth. The results show that while this method is viable, there needs to be more testing and improvements before this method can be used accurately on a CubeSat. There are three main changes that should be researched and implemented before launching a CubeSat with this GNSS-R method:

1. Replace COTS GPS Receiver with Software Receiver

Although the COTS GPS receiver used in this research was successfully able to track reflected GPS signals, this becomes more unreliable as the software behind receiver is unknown. There are also unknowns in whether the two receivers are operating the same way. To mitigate these unknowns, a better way is to use a software receiver where every aspect of the GPS processing is known. This is significantly more work; however, there are many resources available for GPS software receivers. Although software receivers increase the processing load and power consumption, this can be mitigated by using digital signal processors (DSPs) or field-programmable gate arrays (FPGAs).

2. Obtain more accurate estimates of antenna gain patterns, mean square slope, and scat-

tering area

The antenna gains used in producing the results shown were held constant. The antennas used on the quadcopter have low gain and are not directional; however, the exact gain patterns are not known. The difference in gain between small and large incidence angles are only a few dB, but is not negligible when estimating the dielectrics of sea ice. Similarly, the mss is also important in the accuracy of this method as small variations will have an effect on the estimated dielectric constant. The mss can be measured when the specular reflections occur over land; however, it is much harder to so for sea ice in the arctic. Research into sea ice roughness models would benefit the mss estimates for this method. Finally, the scattering area can also make a large impact in the results. This parameter is much more difficult to estimate, so more research needs to be done in this area.

3. Replicate testing in more remote areas while the platform is moving

The location for the experiments conducted in this research is not ideal. There are too many environmental factors contributing to the data recorded with the quadcopter. In order to improve the accuracy of this method, the location should be changed. First, the tests should be done outside the city, preferably in a flat clearing near a larger body of water. This eliminates the effects of trees and buildings that get in the way, as well as removing the effects of uneven terrain on mss and scattering area. Secondly, the ultimate goal for this research is to be able to identify sea ice. This is much more difficult to accomplish from a quadcopter since the temperature at any location with large areas of ice will likely affect the performance of the quadcopter itself.

References

[1] M. Martín-Neira, "A passive reflectometry and interferometry system (PARIS): Application to ocean altimetry," *ESA Journal*, vol. 17, pp. 331–355, 1993.

[2] E. Cardellach, "Sea surface determination using GNSS reflected signals," Ph.D. dissertation, Universitat Politècnica de Catalunya, 2001.

[3] J. L. Garrison, A. Komjathy, V. U. Zavorotny, and S. J. Katzberg, "Wind speed measurements using forward scattered GPS signals," *IEEE Transactions on Geoscience and Remote Sensing*, vol. 40, no. 1, pp. 50–65, 2002.

[4] A. Komjathy, J. Maslanik, V. U. Zavorotny, P. Axelrad, and S. J. Katzberg, "Sea ice remote sensing using surface reflected GPS signals," in *Geoscience and Remote Sensing Symposium*, vol. 7, 2000, pp. 2855–2857.

[5] F. Fabra, "GNSS-R as a source of opportunity for remote sensing of the cryosphere," Ph.D. dissertation, Universitat Politècnica de Catalunya, 2013.

[6] M. Belmonte-Rivas, "Bistatic scattering of global positioning system signals from arctic sea ice," Ph.D. dissertation, University of Colorado, 2007.

[7] M. Belmonte-Rivas, J. A. Maslanik, and P. Axelrad, "Bistatic scattering of GPS signals off arctic sea ice," *IEEE Transactions on Geoscience and Remote Sensing*, vol. 48, no. 3, pp. 1548–1553, 2010.

[8] D. S. Masters, "Surface remote sensing applications of GNSS bistatic radar: Soil moisture and aircraft altimetry," Ph.D. dissertation, University of Colorado, 2004.

[9] S. J. Katzberg, O. Torres, M. S. Grant, and D. Masters, "Utilizing calibrated GPS reflected signals to estimate soil reflectivity and dielectric constant: Results from SMEX02," *Remote Sensing of Environment*, vol. 100, no. 1, 2005.

[10] S. T. Lowe, J. L. LaBrecque, C. Zuffada, L. J. Romans, L. E. Young, and G. A. Hajj, "First spaceborne observation of an earth-reflected GPS signal," *Radio Science*, vol. 37, no. 1, 2002.

[11] C. S. Ruf, R. Atlas, P. S. Chang, M. P. Clarizia, J. L. Garrison, S. Gleason, S. J. Katzberg, Z. Jelenak, J. T. Johnson, S. J. Majumdar, A. O'Brien, D. J. Posselt, A. J. Ridley, R. J. Rose, and V. U. Zavorotny, "New ocean winds satellite mission to probe hurricanes and tropical convection," *Bulletin of the American Meteorological Society*, vol. 97, no. 3, pp. 385–395, 2016.

[12] Navipedia. (2015) Earth sciences. [Online]. Available: http://www.navipedia.net/index.php/Earth_Sciences

[13] N. Snow and I. D. Center. (2016) January hits new record low in the arctic. [Online]. Available: http://nsidc.org/arcticseaicenews/2016/02/january-hits-new-record-low-in-the-arctic/

[14] S. Gleason, "Towards sea ice remote sensing with space detected GPS signals: Demonstration of technical feasibility and initial consistency check using low resolution sea ice information," *Remote Sensing*, vol. 2, no. 8, pp. 2017–2039, 2010.

[15] ESTCube. (2013). [Online]. Available: https://www.estcube.eu/en/home

[16] A. Abdallah. (2014) Iraq launches its first satellite - TigriSat. [Online]. Available: http://www.iraqinews.com/features/iraq-launches-first-satellite-tigrisat/

[17] Yle Uutiset. (2017) Aalto-2: Finland's first satellite launched into orbit. [Online]. Available: https://yle.fi/uutiset/osasto/news/aalto-2_finlands_first_satellite_launched_into_orbit/9571387

[18] BBC News. (2017) Ghana launches its first satellite into space. [Online]. Available: http://www.bbc.com/news/world-africa-40538471

[19] Canadian Satellite Design Challenge. (2017) About CSDC. [Online]. Available: http://www.csdcms.ca/about-csdc/

[20] "Department of defense world geodetic system 1984: Its definition and relationships with local geodetic systems," National Imagery and Mapping Agency, Tech. Rep. 8350.2, 1997.

[21] M. Schenewerk, "A brief review of basic GPS orbit interpolation strategies," *GPS Solutions*, vol. 6, no. 4, pp. 265–267, 2003.

[22] X. Li. (2008) A study on the gps satellites orbit. [Online]. Available: http://ccar.colorado.edu/asen5050/projects/projects_2008/xiaofanli/

[23] K. Borre, D. M. Akos, N. Bertelsen, P. Rinder, and S. H. Jensen, *A Software-Defined GPS and Galileo Receiver: A Single-Frequency Approach*. Basel, Switzerland: Birkhäuser, 2007.

[24] A. J. Van Dierendonck, *Global Positioning System: Theory and Applications*. Cambridge, Massachusetts: American Institute of Aeronautics and Astronautics, 1996, vol. 1.

[25] S. Gleason, "Remote sensing of ocean, ice and land surfaces using bistatically scattered GNSS signals from low earth orbit," Ph.D. dissertation, University of Surrey, 2006.

[26] P. Beckmann and A. Spizzichino, *The Scattering of Electromagnetic Waves from Rough Surfaces*. Oxford, England: Pergamon Press, 1963.

[27] N. Roussel, F. Frappart, G. Ramillien, J. Darrozes, C. Desjardins, P. Gegout, F. Pérosanz, and R. Biancale, "Simulations of direct and reflected wave trajectories for ground-based GNSS-R experiments," *Geoscientific Model Development*, vol. 7, pp. 2261–2279, 2014.

[28] K. M. Larson and F. G. Nievinski, "GPS snow sensing: Results from the Earthscope plate boundary observatory," *GPS Solutions*, vol. 17, no. 1, pp. 41–52, 2013.

[29] S. Jin, E. Cardellach, and F. Xie, *GNSS Remote Sensing: Theory, Methods and Applications*. Dordrecht, Netherlands: Springer, 2014.

[30] V. U. Zavorotny and A. G. Voronovich, "Scattering of GPS signals from the ocean with wind remote sensing application," *IEEE Transactions on Geoscience and Remote Sensing*, vol. 38, no. 2, pp. 951–964, 2000.

[31] "WMO sea ice nomenclature," World Meteorological Organization, Tech. Rep. 259, 1970.

[32] M. R. Vant, R. O. Ramseier, and V. Makios, "The complex-dielectric constant of sea ice at frequencies in the range 0.1-40 GHz," *Journal of Applied Physics*, vol. 49, no. 3, pp. 1264–1280, 1978.

[33] International Telecommunications Union, *Electrical Characteristics of the Surface of the Earth*, 1992, P.527-3.

[34] S. Gleason and D. Gebre-Egziabher, *GNSS Applications and Methods.* Norwood, Massachusetts: Artech House, 2009.